UM HE 91-44

Polarization of the Sigma Minus Hyperon Produced by a Polarized Neutral Particle Beam

An Nhatton Nguyen

FERMILAB
FEB 07 1992
LIBRARY

December 1991

Supported in part by the National Science Foundation

ABSTRACT

POLARIZATION OF THE SIGMA MINUS HYPERON PRODUCED BY A POLARIZED NEUTRAL PARTICLE BEAM

by An Nhatton Nguyen
Dissertation Director: Dr. Michael J. Longo

A spin transfer technique has been tried in an attempt to produce a beam of polarized hyperons. The method makes use of a two-stage targeting scheme where unpolarized protons from Fermilab's Tevatron incident on target number one (Cu) at production angles of ± 2.0 mrad would produce a beam of particles containing polarized Λs, and Ξs as well as neutrons and Ks. This secondary beam would then be swept magnetically to retain only neutral particles and brought to bear on target number two (Cu) at 0.0 mrad, producing a tertiary beam of hyperons, hopefully polarized.

The polarization of some 1.3 millions reconstructed $\Sigma^- \rightarrow n\pi^-$ events in this tertiary beam (the Σ^- having been produced in the inclusive reaction $neutrals + Cu \rightarrow \Sigma^- + X$) has been measured at average Σ^- momenta 320 GeV/c (1.14 millions events) and 410 GeV/c (135,000 events) and found to be $|P| = 3.9 \pm 3.2 \pm 1.8$ % and $|P| = 13.9 \pm 8.1 \pm 2.0$ % respectively, where the first uncertainty is statistical and the second systematic. These polarizations are small and consistent with zero, and preclude a meaningful measurement of the Σ^- magnetic moment. The sign of the polarizations at the target is ambiguous, giving rise to two possible different solutions for the magnetic moment--one of which distinctly disagrees with the world average value for the moment. However, this solution fits the data slightly better than the other. This inconsistency would not exist if the polarization is, in fact, zero.

POLARIZATION OF THE SIGMA MINUS HYPERON PRODUCED BY A POLARIZED NEUTRAL PARTICLE BEAM

by

An Nhatton Nguyen

A dissertation submitted in partial fulfillment
of the requirements for the degree of
Doctor of Philosophy
(Physics)
in The University of Michigan
1991

Doctoral Committee:

Professor Michael J. Longo, Chairman
Research Scientist Richard H. Gustafson
Professor Ctirad Uher
Professor Nguyen X. Vinh
Professor David N. Williams

DEDICATION

To all of my loving family.

ACKNOWLEDGMENTS

This thesis could not have been written if my advisor, Mike Longo, had not allowed, introduced, and made it possible for me to work on data analysis for Fermilab experiment E756. I owe Mike much more than this, of course. At times during my work on a previous project under his guidance, he had been almost like a father to me, providing much support, encouragement, and gentle prodding to keep me on the right path.

One of the people of E756 whom Mike introduced me to is Kam-biu Luk. If Mike had been like a father to me, Kam-biu had been like a second advisor to me during my stay at Fermilab, guiding and assisting me in every possible ways--from providing a workstation, to dealing with the bureaucracy, to answering a multitude of physics questions. Most importantly, he is a never-ending source of inspiration by the sheer virtue of his single-minded and enthusiastic devotion to physics. Had I have the occasion to work with Kam-biu at a much earlier stage of my graduate education, perhaps I would have taken the other path at this particular fork in my life.

Pak-ming Ho is another close E756 friend I've made. Over time, our friendship has grown and Ming has become the big brother I never have. This thesis is as much Ming's as it is mine (but I alone am responsible for any blemishes and deficiencies). I profited greatly from the many physics discussions I had with Ming as well as learned much from him of the art world and opera and jazz and *haute* Chinese *cuisine.* Without Ming's constant urgings and practical advice, too, this thesis could not have been completed in a reasonable amount of time.

Many thanks go to the other members of the E756 collaboration, without whom and whose hard work there would have been no data for this thesis: K. Heller, G. Thomson, K. Johns, R. Rameika, C. James, J. Duryea, H. T. Diehl, G. Guglielmo, and Y. Zou.

The completion of the data analysis would have been extremely difficult were it not for the generous help and excellent resources kindly provided by Fermilab's computing division. Specifically, thanks go to J. Nicholls, T. Nguyen, and M. Stolz.

Many friends at Fermilab helped make cloudy days less cloudy, and sunshiny days more sunshiny. My heartfelt appreciation goes out to anh chi Thinh Pham and family; Ai and Trang and Anson Nguyen; my "adopted mom", Liz Duty; the Mulveys: Jim, Linda, Ted, and Valerie.

The same appreciation belongs to many other friends and associates who have helped my physics enterprise by providing their friendship and encouragements in one way or another over the years: Prof. A. Varone (who introduced me to the natural sciences as far back as grade school, gave me my first slide rule and tons and tons of good chemistry, and physics, and astronomy books), Betty Dimitry, Joyce Pagano, Patricia Couture (who went out of her way to obtain materials for a laser I was building), Robert Acquarelli, Scott Peacor, Anup Majumder, Curtis Weaverdyck and family, Helmut Schick, Jim Pluta, Dennis Allen, Alex Kim, Kael Hanson, James and Alicia Renfrew.

Long though this acknowledgment is, I cannot resist the temptation to add one more note of thanks. The circumstances surrounding the completion of this work let me be privy to revelations from friends and foes alike--which revelations they would not have made otherwise and which have taught me much in the manners of men and mores. These constitute an education in themselves. This thank-you note is a testimonial tribute to those who have made that education possible.

Last and most important, all of my works, this thesis included, could never--never ever--have borned fruits without the spiritual and material support, the uncountably many sacrifices, the infinite patience, and the constant encouragement of all the members of my family: both of my grandmothers, parents, brothers, and so many uncles and aunts and cousins.

TABLE OF CONTENTS

DEDICATION ii

ACKNOWLEDGMENTS iii

LIST OF FIGURES vii

LIST OF TABLES x

CHAPTER

INTRODUCTION 1

1.1 Hyperon production polarization 3

1.2 Magnetic Moment 6

1.3 Theoretical Models for Polarization and Magnetic Moment 9

APPARATUS 13

2.1 Experimental beam and targets 13

2.2 Collimator 16

2.3 Spectrometer 19

2.4 Trigger logic and data acquisition 23

2.5 Calibration 23

EVENT RECONSTRUCTION AND SELECTION 26

3.1 Event Reconstruction 26

3.2 Event Selection 33

POLARIZATION ANALYSIS 45

4.1 Introduction 45

4.2 Method....48
4.2.1 Graphical Method....48
4.2.2 Hybrid Monte-Carlo Method....52
4.2.3 Bias....56
4.3 The Grand $\chi 2$ Fit....57

RESULTS AND CONCLUSION....59
5.1 Introduction....59
5.2 Results--Graphical Method....59
5.2 A Digression
Graphical Method and the y Component....65
5.3 Results--Hybrid Monte-Carlo Method....67
5.4 Conclusion....74

REFERENCES....76

LIST OF FIGURES

Figure

1.1 The spin transfer scheme used by Fermilab experiment E756 to produce a polarized hyperon beam. 2
1.2 Polarization at target. 5
1.3 Polarization of hyperons as a function of transverse momentum. 6
1.4 Experimental measurements of the magnetic moment of the Σ^-. 9
1.5 DeGrand and Miettinen model. 10
1.6 Lund model. 11
2.1 Schematic beam line set up (not to scale) 14
2.2 Schematic (a) plan and (b) elevation view (not to scale) of a proton beam hitting the upstream target with a vertical production angle of -2.0 or +2.0 mrad, and the secondary neutral beam hitting the second target at 0.0 mrad. 14
2.3 Schematic (a) plan and (b) elevation view of a neutral beam passing through a sweeper magnet to strike the downstream target at 0 mrad production angle and then on through the collimator. 15
2.4 (a) Bend view (b) non-bend view (magnetic field of M1 perpendicular to this plane) of the collimator 17
2.5 Cross sections of the collimator. 18
2.6 Channel acceptance of the collimator at different magnet currents. 19
2.7 Plan view of the spectrometer. 20
2.8 Block diagram for the readout circuit of a single MWPC channel. 25
3.1 Single track topology for the case of the Σ^- (a)bend,(b) non-bend view 27
3.2 Virtual source point used in the bend-view reconstruction of the upstream track 29
3.3 Distribution of geometric χ^2. 30
3.4 Distribution of kinematic χ^2 for a typical run. 32

3.5 Distribution of the parent's (upstream track's) momentum after χ^2 cut for -450A sample at negative production angle. 35
3.6 Distribution of the z position of the decay vertex after χ^2 and momentum cuts for -450A sample at negative production angle. 35
3.7 Projections of the upstream track at the exit aperture of the hyperon magnet for -450A sample. 36
3.8 Distribution of Σ^--π^- opening angle for -450A sample at negative production angle. 37
3.9 Candidate Σ^- events (reconstructed under the hypothesis $\Sigma^- \rightarrow n\pi^-$) after all but the mass cut for -450A sample at negative production angle. 39
3.10 Monte-carlo $\Xi^- \rightarrow \Lambda\pi^-$ events reconstructed as $\Sigma^- \rightarrow n\pi^-$ events show a sharp drop off at a distance $\approx 5\ \sigma$ (at the arrow) from the Σ^- mass peak. 41
3.11 Missing mass distribution with the charged daughter assumed to be a π^- and the parent to be a Ξ^- , (a) before all cuts, (b) after all cuts for 450A sample at negative production angle. 42
3.12 Missing mass distribution, before any cuts, with the charged daughter assumed to be a π^- and the parent, a K^-. No apparent π^0 peak (at 135 MeV/c2)can be seen. 43
4.1 $(1+\alpha P \cos\theta)$ vs. $\cos\theta$ for $\alpha P < 0$, $\alpha P = 0$, $\alpha P > 0$. 49
4.2 $\cos\theta_x$ distribution (real events and internal monte-carlo events) for negative production angle. 50
4.3 $\cos\theta_z$ distribution (real events and internal monte-carlo events) for negative production angle. 51
4.4 $\cos\theta_y$ distribution (real events and internal monte-carlo events) for negative production angle. 51
5.1 Ratio R for (a) x view (b) z view, for the -450A data set. 61
5.2 Ratio R for (a) x view (b) z view, for the -1000A data set. 62
5.3 Ratio R for (a) x view (b) z view, for the mixtures of equal parts from the positive and the negative angle data sets (-450A) 63

5.4 Comparison of the ratio R for (a) x view (b) z view, between the normal data set and the mixture data set of equal parts of positive and negative angle events (all data at -450A). 64
5.5 Ratio R for y view for -450A data set. 66
5.6 Ratio R for y view for mixtures of equal parts positive and negative production angle from the -450A data set. 67
5.7 Precession angle versus field integral for the two solutions (A & B) found using the hybrid method....72
5.8 Final solutions A (right hand picture) and B (left hand picture) correspond essentially to an unresolved ambiguity in the initial polarization direction at target. 72

LIST OF TABLES

Table

1.1 Prediction for baryon magnetic moments by different models. 13

2.1 Field integrals and transverse momentum change at different sweeper currents 16

2.2 (a) Z-position, aperture dimensions, and pitch of SSDs and multiwire chambers (b) Dimensions of scintillation counters 21

3.1 Description of different classes of events in the reconstruction program. The percentages give the number of original data sample belonging to each class 31

3.2 Typical distribution of percentage of events cut out by the different event-selection cuts. 40

3.3 The final distribution of events under various running conditions. 40

5.1 Linear regression fits of the data of the graphs of Figures 5.1-3 to $R_j=\alpha P_j\cos\theta_j$. The number of degrees of freedom is 19. 60

5.2 Results for the magnitude of the asymmetry $|\alpha P|$ and polarization $|P|$ that follow from the linear regression fits of Table 5.1. 65

5.3 Results for the components of the polarizations, biases, and χ^2 for the positive and negative production angle data (number of degrees of freedom is 20) for the hybrid monte-carlo method, calculated with Equation 4.23 68

5.4 Results for the magnitude of the polarization signal at target, $|\alpha P|$, using the hybrid monte-carlo method. 68

5.5 Results for the precession angle ϕ and its error 79

5.6 Results for the asymmetry αP, and the x and z biases when both the -450A and -1000A samples were fitted simultaneously using the

"grand-χ^2". Two separate fits are shown: first, with g/2 being a free parameter and second, with g/2 set at the world value. 70

5.7 Results for the polarization P, precession angle ϕ, and magnetic moment μ when both the -450A and -1000A samples were used in simultaneous fits using the "grand-χ^2" 71

5.8 Predicted polarization asymmetries for various spin-transfer reactions with a neutral beam. 75

CHAPTER 1

INTRODUCTION

Measurements of hyperon production polarization and magnetic moment have continually provided clues to baryon composition and structure. Ever since the discovery in 1976 that the Λ^0 (and later Ξ's and Σ's) hyperons are spin-polarized in inclusive reactions of the type, *proton +nucleon* $\rightarrow$ *hyperon* + *X*, where X represents undetected particles,[1] experiments have unceasingly turned up one surprise after another, culminating in the latest one in 1990: the polarization of the $\bar{\Xi}^+$'s is comparable to that of the Ξ^-'s.[2]

Of the many methods--e.g. magnetic resonance, spectral analysis of exotic atoms, and Primakoff effect--that have been used to make these magnetic moment measurements, the spin-precession method has been the most popular as well as the most productive. For this method to work, however, a polarized beam of the particles under study must be secured.

To this end, one technique has been tried recently. It makes use of a two-stage targeting scheme in an attempt to obtain a polarized beam of hyperons (see Figure 1.1). The idea was that unpolarized protons from Fermilab's Tevatron incident

on target number one would produce a polarized beam of particles that was then magnetically swept to retain only neutral particles. This secondary beam would then be brought to bear on target number two, producing a tertiary beam. Hopefully, in this process, the spin information of the neutrals would be communicated to some of the hyperons in the tertiary beam, so that they would also be polarized.

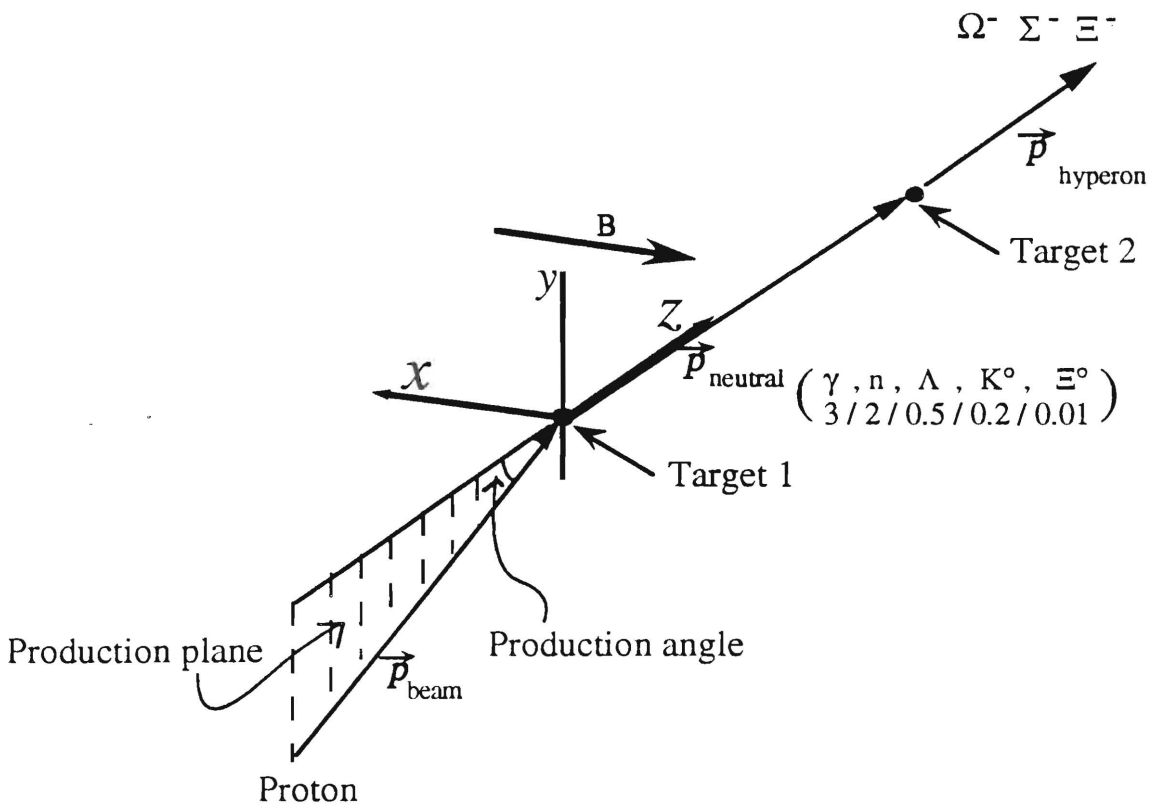

Figure 1.1 The spin transfer scheme used by Fermilab experiment E756 to produce a polarized hyperon beam. A magnetic field **B** in the region between target 1 and target 2 was used to sweep the secondary beam, retaining only the neutral particles in this beam. The ratio of different particle species in the neutral beam is indicated.

This so-called spin transfer method has been used successfully by Fermilab experiment E756 to produce a polarized beam of Ω^- particles and, thereby, to make the first statistically significant measurement of the, previously elusive, Ω^- magnetic moment.[3] Also measured in this experiment using this method was the magnetic moment and /or the polarization of the Σ^-, Ξ^-, among others. The polarization of the Σ^- will be reported in what follows.

1.1 Hyperon production polarization

Even without using the spin transfer method, most hyperons are produced spin-polarized in inclusive reactions of the type *proton +nucleon* $\rightarrow$ *hyperon* + *X*, as mentioned above.[1,4-10] By contrast, the *anti* -hyperons, $\bar{\Lambda}$ and $\bar{\Xi}^0$, have polarizations consistent with zero or inconclusive respectively.[11-14] The usual method of production is illustrated in Figure 1.2. The incoming beam of unpolarized protons strikes a target (usually beryllium, but copper and other materials have also been used) at an angle (the "production angle"), producing the outgoing hyperon beam along the z axis of the coordinate system shown. The plane defined by the normal, $(\mathbf{p}_{beam} \times \mathbf{p}_{hyperon})/|\mathbf{p}_{beam} \times \mathbf{p}_{hyperon}|$, is called the production plane, where $\mathbf{p}_{beam}$ is the momentum vector of the proton beam, and $\mathbf{p}_{hyperon}$ the hyperon beam.

Parity conservation in strong interactions requires that if the hyperon beam is polarized, its polarization vector must be normal to the production plane. Formally, the polarization vector is defined in the direction where the expectation value of the spin components of an ensemble of particles is maximum--i.e.

$$\mathbf{P} = |\mathbf{P}|\mathbf{e}_0 \tag{1.1}$$

where $\mathbf{e}_0$ is the particular unit vector, $\mathbf{e}$, that maximizes the expectation value

$$\langle \mathbf{S} \cdot \mathbf{e} \rangle$$

where S is the spin, and the degree of polarization (or just polarization) |P| is the value of this expectation value

$$|P| = \max\langle \mathbf{S}\cdot\mathbf{e}\rangle = \langle \mathbf{S}\cdot\mathbf{e}_0\rangle \tag{1.2}$$

P can be expressed generally in terms of an orthogonal right-handed coordinate system formed from the physical vectors available, namely $\mathbf{p}_{beam}$ and $\mathbf{p}_{hyperon}$, as

$$\mathbf{P} = f\mathbf{p}_{hyperon} + g\left(\mathbf{p}_{beam} \times \mathbf{p}_{hyperon}\right) + h\left[\left(\mathbf{p}_{beam} \times \mathbf{p}_{hyperon}\right) \times \mathbf{p}_{hyperon}\right] \tag{1.3}$$

The coefficients f=h=0 necessarily since **P** must be a pseudovector to make its scalar product with **S**, another pseudovector, invariant under spatial coordinate inversion--i.e. under parity transformation. The convention used here is that **P** is positive if it is parallel to ($\mathbf{p}_{beam}$ x $\mathbf{p}_{hyperon}$). Also, the production angle is positive if ($\mathbf{p}_{beam}$ x $\mathbf{p}_{hyperon}$) is parallel to the x axis, using the coordinate system shown in Figure 1.2. The important thing physics-wise is that the direction of polarization is reversed if the production angle is reversed. This fact allows systematic effects, called biases, that do not change with a reversal in production angle to be canceled out by comparing data at positive production angle with data at negative angle.

The hyperon production process in the beam fragmentation region generally is thought to be the fragmentation of the proton projectile into its valence quarks and the recombination of these valence quarks with one or two s quarks from the sea. (The case of the Ω^- is special: all three of its valence quarks are promoted from the sea.) In this picture, the polarization of the hyperon could be the result of some sort of leading-particle effect--i.e. observables such as spin alignment and cross section of the product particle are somehow enhanced because the parent and daughter particles have some valence quarks in common. Moreover, the spin (polarization) information of the outgoing particle is thought to be carried by the s quarks. Various models using this picture indicated that the spin of the hyperon is in the same direction as the s quarks for Λ, Ξ^0, Ξ^-, and Ω^-, and opposite for Σ^+, Σ^0, and Σ^-. And in fact, this is born out by

available experimental data on hyperon polarization (see Figure 1.3, which shows the polarization as a function of the transverse momentum, P_t, with $P_t \approx p_{hyperon} \times \theta_{prod.}$ and θ_{prod} is the production angle) of the hyperons.

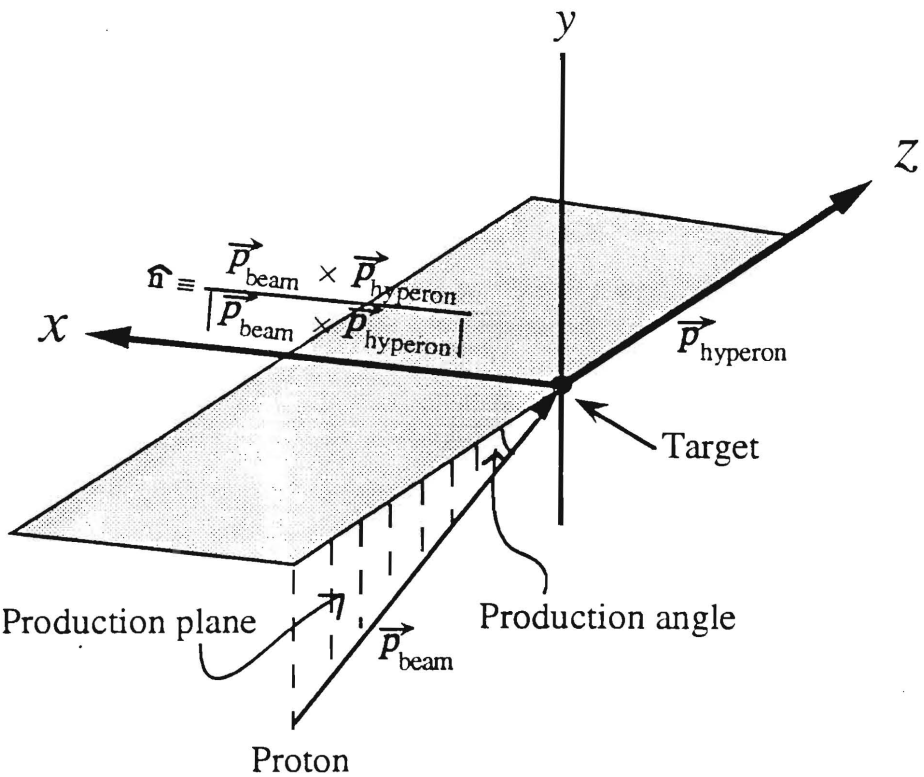

Figure 1.2 Polarization at target.

In E756, a neutral beam, containing mostly γ's, neutrons and less abundant Ξ^0's and Λ's, that had been polarized in this way was permitted to strike a second target head-on, producing a tertiary beam. The incoming neutral hyperons and the outgoing hyperons superficially shared at least one valence s quark. Thus, it was hoped that the s quark(s) would carry the spin information in the neutral beam over to the tertiary beam. And indeed, it turned out that the Ξ^- and Ω^- in the tertiary beam were polarized comparably to the parent neutrals. This fact was utilized with success to measure the magnetic moment of the Ω^-, Ξ^-. [3]

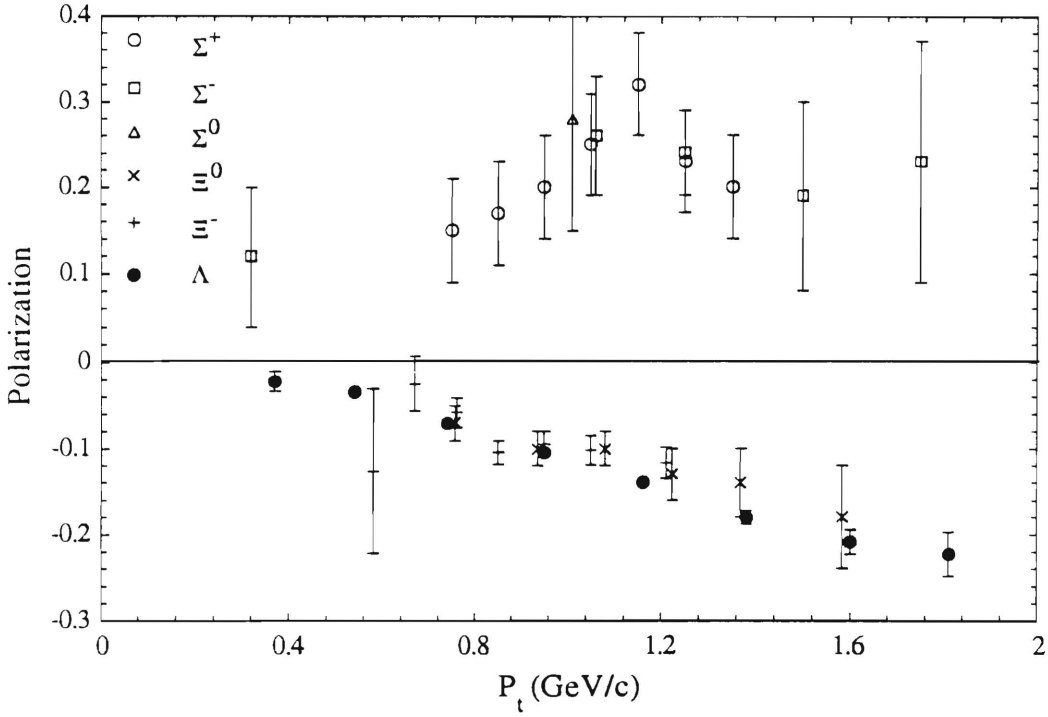

Figure 1.3 Polarization of hyperons as a function of transverse momentum. For Λ polarization at 400 GeV/c and 7.2 mrad production angle, see Ref. 11; for Ξ^- at 400 GeV/c and 5 mrad on Be target, see Ref. 8; Ξ° at 400 GeV/c and 7.2 mrad on Be target, Ref. 5; Σ^- at 400 GeV/c on Cu target, Ref.7; Σ°at 28.5 GeV/c on Be target, Ref.9; Σ^+ at 400 GeV/c and 5 mrad on Be target, Ref.4.

1.2 Magnetic Moment

Since the spin polarization vector is defined in terms of expectation values, by virtue of Ehrenfest's Theorem, its evolution can be described by a classical equation. For the case at hand, this equation is the Bargmann-Michel-Telegdi (BMT for short) equation describing the precession of the "spin four-vector" s_μ (with **s** being the regular spin vector and s_0=0 in the rest frame) of a particle moving in a homogeneous electromagnetic field:[15]

$$\frac{ds}{d\tau}=g\mu_0\left[F\cdot s+(s\cdot F\cdot u)u\right]-\left[\frac{du}{d\tau}\cdot s\right]u \tag{1.4}$$

where $F^{\mu\upsilon}$ is the electromagnetic field tensor, u_μ the four-velocity of the particle, τ the proper time, and $g\mu_0|s|$ the magnetic moment of the particle.

The rate of change of the direction of the polarization vector can be derived from the BMT equation. It is

$$\frac{d\phi_R}{dt}=\mathbf{E}\cdot\mathbf{n}\left(g\mu_0\beta-\frac{e}{m\beta}\right)+\left(g\mu_0-\frac{e}{m}\right)\mathbf{t}\cdot\mathbf{B}\times\mathbf{n} \tag{1.5}$$

where $d\phi_R/dt = (1/\gamma)d\phi_R/d\tau$, $\gamma=(1-\beta^2)^{-1/2}$, $\boldsymbol{\beta}$ is the velocity of the particle (speed of light $c=1$); $\mathbf{E}$ and $\mathbf{B}$ are the electric and magnetic field respectively; and $\mathbf{n}$ and $\mathbf{t}$ are unit vectors such that $\mathbf{t} = \boldsymbol{\beta}/\beta$ and $\mathbf{n}\cdot\mathbf{t}=0$; and ϕ_R is the angle between $\boldsymbol{\beta}$ and the polarization vector in the rest system of the particle.

For the case where there is only a magnetic field perpendicular to the path of the particle--that is, $\mathbf{E}=0$, $\mathbf{B}=|\mathbf{B}|(\mathbf{n} \times \mathbf{t})$--this equation reduces to

$$\frac{d\phi_R}{dt}=\left(g\mu_0-\frac{e}{m}\right)|\mathbf{B}| \tag{1.6}$$

or, after an integration over the path l of the particle,

$$\Delta\phi_R=\frac{1}{\beta}\left(g\mu_0-\frac{e}{m}\right)\int|\mathbf{B}|\cdot dl \tag{1.7}$$

For charged particles, the magnetic moment is related to the charge of the particle as

$$g\mu_0|\mathbf{s}| = g|\mathbf{s}|\frac{e}{2m} \tag{1.8}$$

so that

$$\Delta\phi_R = \frac{e}{\beta m}\left(\frac{g}{2} - 1\right)\int |\mathbf{B}|\cdot dl \tag{1.9}$$

where $\beta \approx 1$ for the experimental conditions of this thesis.

This equation is the basis of the spin-precession method: the magnetic moment of a particle can be obtained immediately by measuring the angle of precession, $\Delta\phi_R$, of a particle in a magnetic field $\int Bdl$. To find $\Delta\phi_R$, the particle is allowed to decay after the precession and its angular decay distribution measured. From the observed asymmetry in the decay distribution, the final orientation of the polarization vector can be deduced and hence the change in its orientation, $\Delta\phi_R$. This is possible because, as will be shown in Chapter 4, in the parity-violating weak decay of the hyperons (e.g. $\Sigma^- \rightarrow n\pi^-$) the angular decay distribution is related to the polarization vector as

$$\frac{dn}{d\Omega} = \frac{1}{4\pi}(1 + \alpha \mathbf{P}\cdot\mathbf{q}) \tag{1.10}$$

where $\mathbf{q}$ specifies the direction of flight of one of the daughter particles, and α is a constant that characterizes the decay.

Figure 1.4 summarizes the experimental status for the measurement of the magnetic moments of the Σ^-.[6,7,16,17] The errors shown include systematic as well as statistical. The Hertzog result alone makes use of the exotic atom technique where atoms consisting of a hyperon and a heavy nucleus were formed and the fine structure splitting (which is proportional to the g-factor) in the x-rays emitted was measured. All other results come from Fermilab hyperon beam experiments (experiment designations are indicated on the graph) that used the spin precession technique. The weighted mean for the Σ^- magnetic moment is -1.157 ± 0.025 n.m..

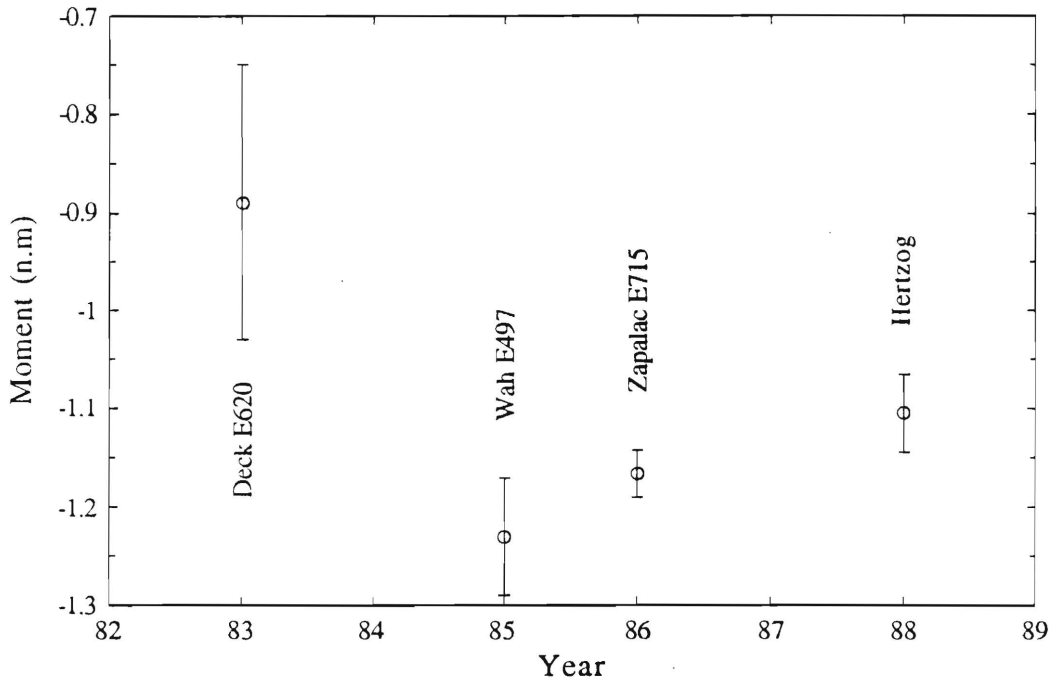

Figure 1.4 Experimental measurements of the magnetic moment of the Σ^-.

1.3 Theoretical Models for Polarization and Magnetic Moment

Polarization models: As was mentioned, in the beam fragmentation picture of the hyperon production process, the s quark(s) picked up from the sea is thought to be the main conveyor of spin and polarization information. Exactly how this comes to be, how the s quarks acquire polarization in the process is the subject of many semi-classical models.

One such model, proposed by DeGrand and Miettinen, suggests that the polarization of the s quark is due to a Thomas precession effect.[18] When a slow-moving s quark from the sea of the proton projectile combines with the valence quarks of the same to form the outgoing hyperon, it experiences an acceleration and a change

in momentum from s/p to s/hyperon as depicted in Figure 1.5 below. This means it is being accelerated by a force **F** representing the color field. Generally, the velocity **v** of the sea s quark is not in the same direction as **F**. This gives rise to a Thomas precession term in the Hamiltonian

$$U \propto \mathbf{s} \cdot (\mathbf{F} \times \mathbf{v}) \tag{1.11}$$

Minimum energy consideration would thus favor the state where the spin vector **s** of the quark and $(\mathbf{F} \times \mathbf{v})$ point in opposite directions (**s** into the page in Figure 1.5). Similar reasoning applied to the fast-going valence quarks or diquarks in the proton (which must decelerate to form the outgoing hyperon) indicates that their spin orientation will be opposite to that of the s quark. This explains correctly the direction of polarization with respect to the production plane and the empirical fact that leading spectators prefer to recombine with spin up while the sea partons prefer spin down.

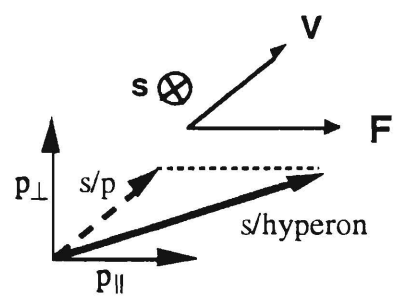

Figure 1.5 DeGrand and Miettinen model.

Another model, proposed by Andersson, Gustafson, and Ingelman of LUND, theorizes that when the proton projectile breaks up in the fragmentation process, the stretched color field of the remaining valence quark creates a massive quark-antiquark pair from the vacuum.[19] The pair is created a finite distance l apart with one particle having momentum $\mathbf{k}_\perp$ and the other $-\mathbf{k}_\perp$, so that together the pair has a finite angular momentum, **L**. Local conservation of momentum then dictates that the spin **s** of the

pair must be equal and opposite to L. This model can thus explain the $\mathbf{p}_\perp$ dependence of hyperon polarization--namely, $P \propto \mathbf{p}_\perp$ for small $\mathbf{p}_\perp$--because the larger $\mathbf{p}_\perp$, the larger s must be to compensate L. It also explains qualitatively the sign of the polarization.

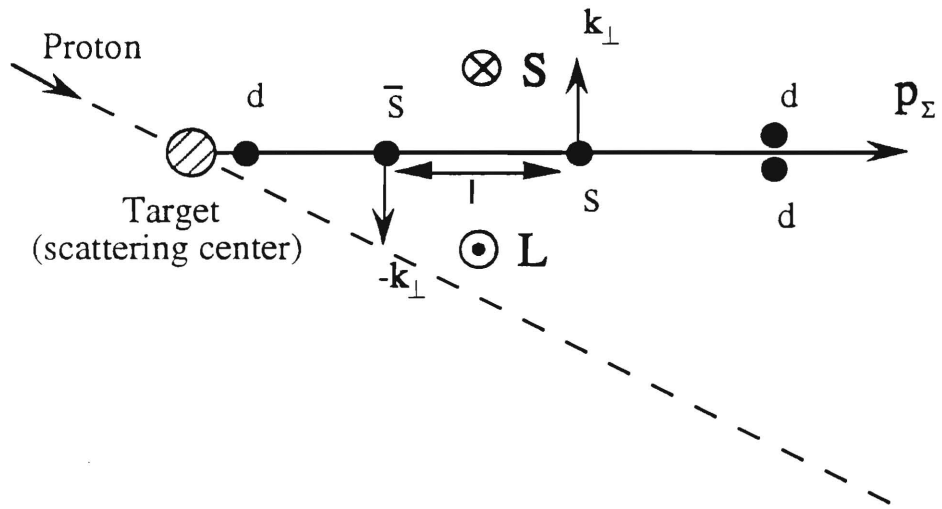

Figure 1.6 Lund model.

A quantitative prediction for the magnitude of the polarization is put forth in a model for the Λ polarization by J. Szwed.[20] In the model, the sea quark gets polarized by multiple scattering in the color field in much the same way as electrons in a Coulomb field. The model incorporates the subsequent hadronization of the sea quark with the quark recombination model. The result for the polarization P is that

$$P \propto \alpha_s \frac{m_s}{E_s^2} |\mathbf{k}_\perp| \tag{1.12}$$

where α_s is the strong coupling constant; m_s, E_s, and $\mathbf{k}_\perp$ are the mass, energy, and transverse momentum of the s quark respectively; and it explains the polarization of the Λ fairly well. It needs to be extended to other hyperons, however.

Magnetic moment models: In the static, naive broken SU(6) quark model, the magnetic moment of the hyperon is given simply by

$$\mu_{hyperon} = \left\langle \Psi_{hyperon} \middle| \sum_{valencequark} \mu_{quark} \middle| \Psi_{hyperon} \right\rangle \tag{1.13}$$

where μ_{quark} are the quark moment operators and $\psi_{hyperon}$ is the hyperon wavefunction. Thus, for example, using the wavefunction for the Σ^-

$$\Psi_{\Sigma^-} \uparrow = \left[\sqrt{\frac{2}{3}} d \uparrow d \uparrow s \downarrow - \sqrt{\frac{1}{6}} (d \uparrow d \downarrow + d \downarrow d \uparrow) s \uparrow + \text{flavor permutations} \right] \times \text{color singlet} \tag{1.14}$$

one gets, for the Σ^- magnetic moment

$$\mu_{\Sigma^-} = \frac{4}{3} \mu_d - \frac{1}{3} \mu_s \tag{1.15}$$

Table 1.1 summarizes the naive SU(6) static quark model for other hyperon magnetic moments. For comparison, nominal experimental values up to date are included in the table.[21]

BARYON	Static SU(6) Quark Model Prediction (n.m.)		Experiment(n.m.)
p	$4/3\mu_u - 1/3\mu_d$	= input	2.793
n	$4/3\mu_d - 1/3\mu_u$	= input	-1.913
Λ	μ_s	= input	-0.613 ± 0.004
Σ^+	$4/3\mu_d - 1/3\mu_s$	= 2.673 ± 0.001	2.419 ± 0.022
$\Sigma^0 \rightarrow \Lambda$	$1/\sqrt{3}(\mu_d - \mu_u)$	= -1.63 ± 0.001	-1.61 ± 0.08
Σ^-	$4/3\mu_d - 1/3\mu_s$	= -1.091 ± 0.001	-1.157 ± 0.025
Ξ^0	$4/3\mu_s - 1/3\mu_u$	= -1.435 ± 0.005	-1.253 ± 0.014
Ξ^-	$4/3\mu_s - 1/3\mu_d$	= -0.493 ± 0.005	-0.675 ± 0.022
Ω^-	$3\mu_s$	= -1.839 ± 0.012	-2.00 ± 0.15

Table 1.1 Prediction for baryon magnetic moments by naive static SU(6) quark model and latest experimental values for the same.

CHAPTER 2

APPARATUS

2.1 Experimental beam and targets

Experiment E756 occupied the Proton Center beam line at Fermilab. The beam line carried an 800 GeV/c primary proton beam, produced by the Tevatron in spills of 20-seconds duration (per one-minute cycle), to the Proton Center target area.

There the beam was focused, steered, and brought to incidence on a copper target (0.5 inch diameter by 1 interaction length = 6 inch) at vertical production angles of ±2.0 mrad and 0.0 mrad with a series of quadrupole and dipole magnets (Figures 2.1 and 2.2). The proton beam, on interaction with the target, produced a secondary beam of particles that was allowed subsequently to pass through a straight magnetic channel placed directly after the target. As the channel was embedded in a dipole magnet, it effectively selected and passed only neutral particles. Further, the field of the dipole was perpendicular to the production plane and so would not precess any possible polarization of the neutral beam (Figure 2.3). This secondary neutral beam

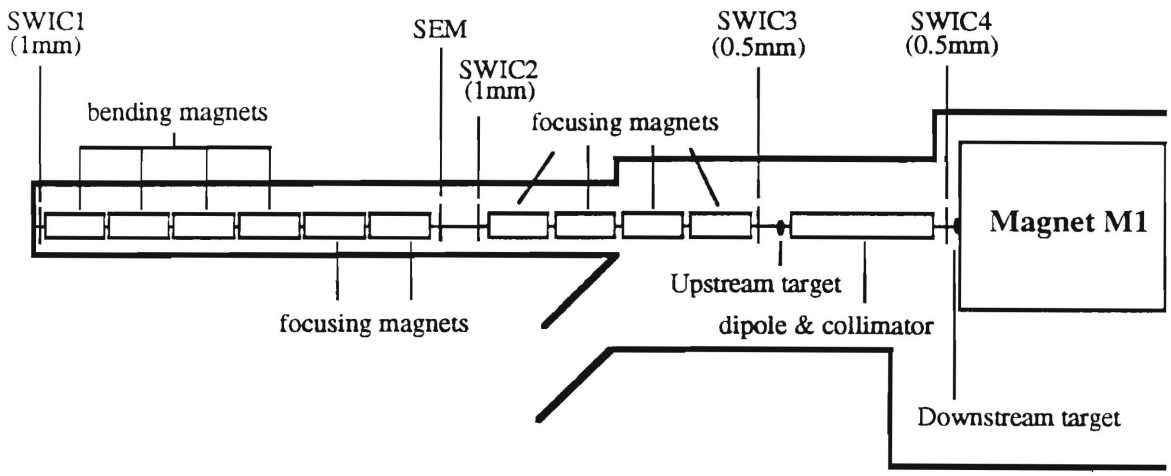

Figure 2.1 Schematic beam line set up (not to scale)

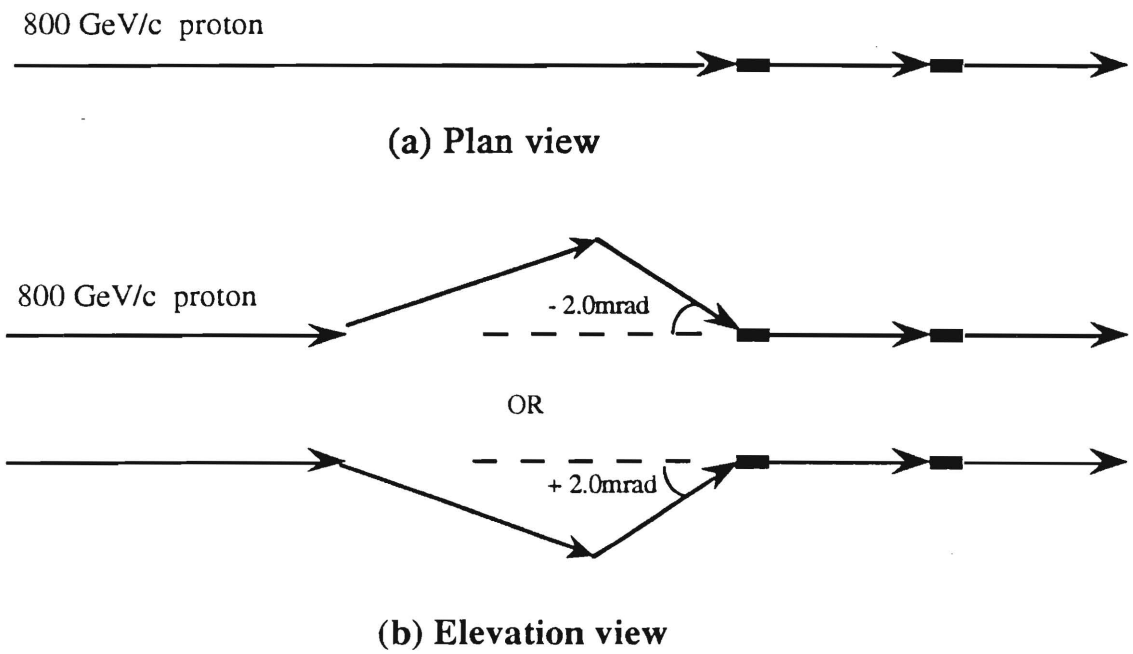

Figure 2.2 Schematic (a) plan and (b) elevation view (not to scale) of a proton beam hitting the upstream target with a vertical production angle of -2.0 or +2.0 mrad, and the secondary neutral beam hitting the second target at 0.0 mrad.

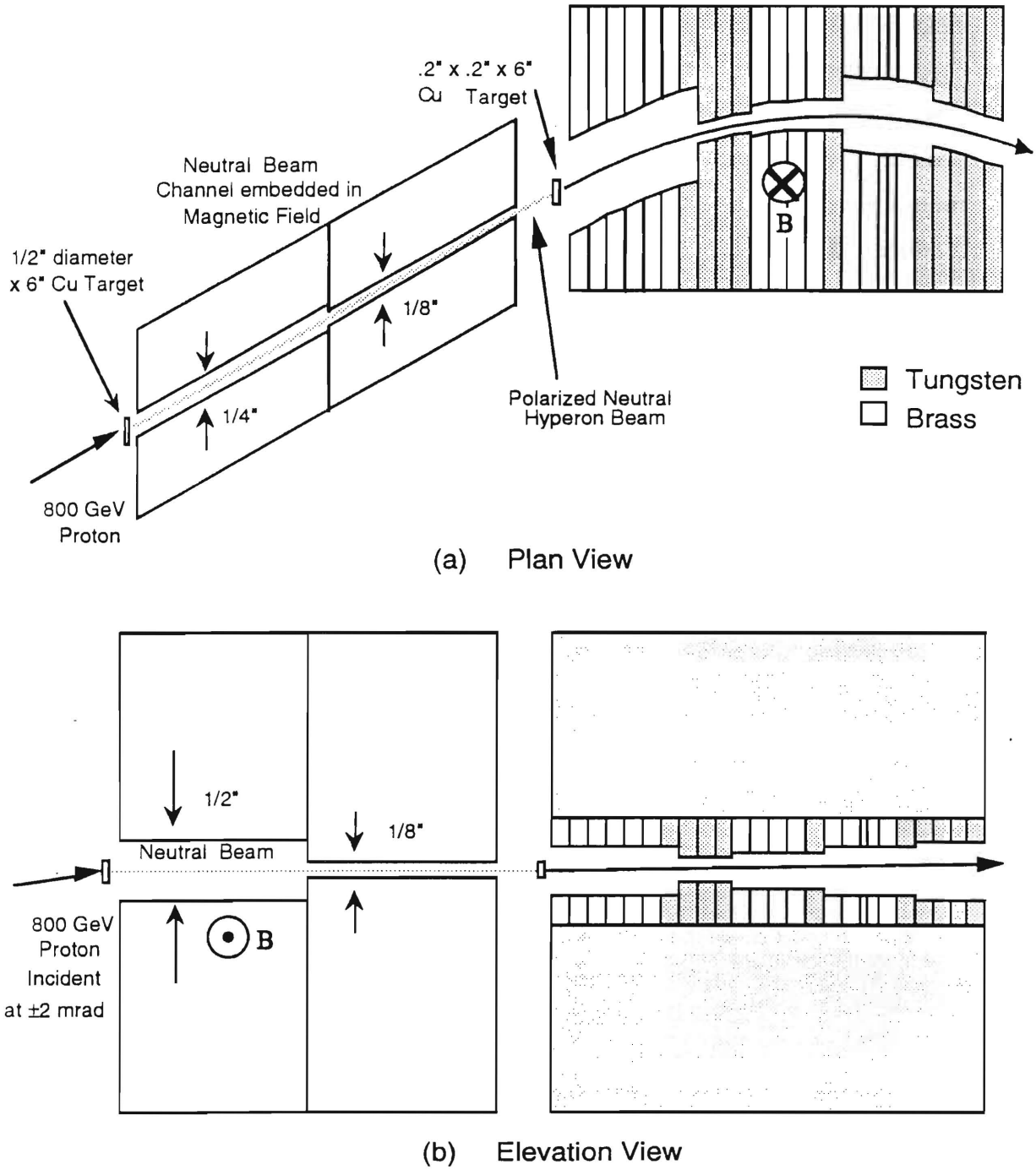

Figure 2.3 Schematic (a) plan and (b) elevation view of a neutral beam passing through a sweeper magnet to strike the downstream target at 0 mrad production angle and then on through the collimator. Magnetic field directions are shown.

was then allowed to impinge squarely (0.0 mrad vertical production angle) on a second copper target located directly in front of a curved magnetic channel--the collimator--which defined and momentum-selected a tertiary beam of charged particles. The position and intensity of the neutral beam as well as the primary proton beam were monitored with segmented-wire-ion-chambers (SWICs) and secondary-emission-monitor (SEMs) respectively.

Subsequently, the decay of Σ^- and other particles contained in this beam were detected and analyzed with a conventional spectrometer consisting of scintillation counters, silicon strip detectors, and multiwire proportional chambers.

2.2 Collimator

The curved channel of the collimator was delineated and carved out with a series of brass and tungsten blocks, embedded in a 7.31 meter long dipole magnet (Figures 2.4 and 2.5). The tungsten blocks were positioned at strategic positions to serve as a dump for beam particles swept off the centerline of the channel by the magnetic field. The defining aperture (the narrowest part) of the channel was 5 X 5 mm^2.

Particles that did go through the channel underwent a bend angle of 14.7 mrad and a change in transverse momentum ("ptkick") the magnitude of which depends on the magnet's excitation current (Table 2.1). The fields were measured with a Hall probe, whence field integrals can be obtained with an estimated uncertainty of 1%.

Current (A)	Field Integral , $\int Bdl$ (T·m)	Ptkick, $e\int Bdl$ (GeV/c)
-450	-14.48	4.343
-750	-17.88	5.364
-1000	-19.44	5.833

Table 2.1 Field integrals and transverse momentum change at different sweeper currents.

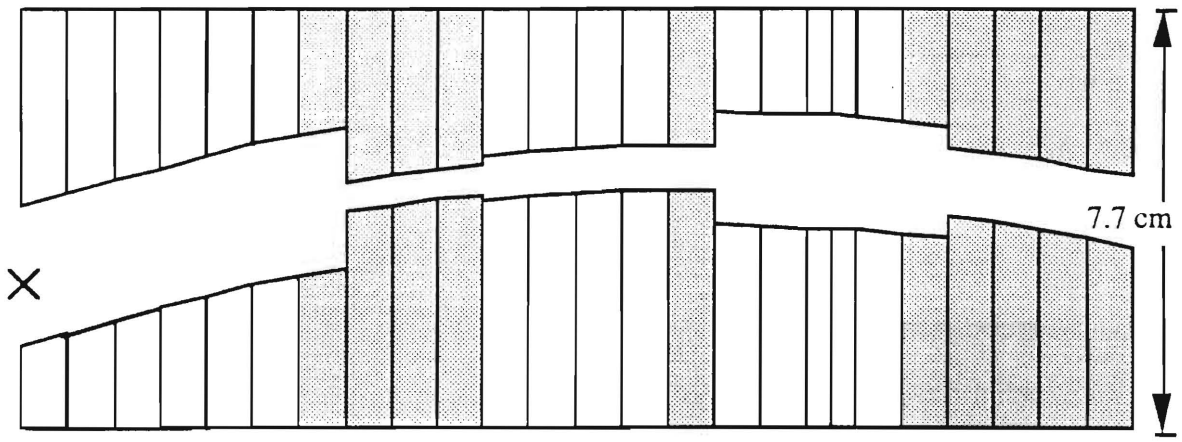

(a) Bend view

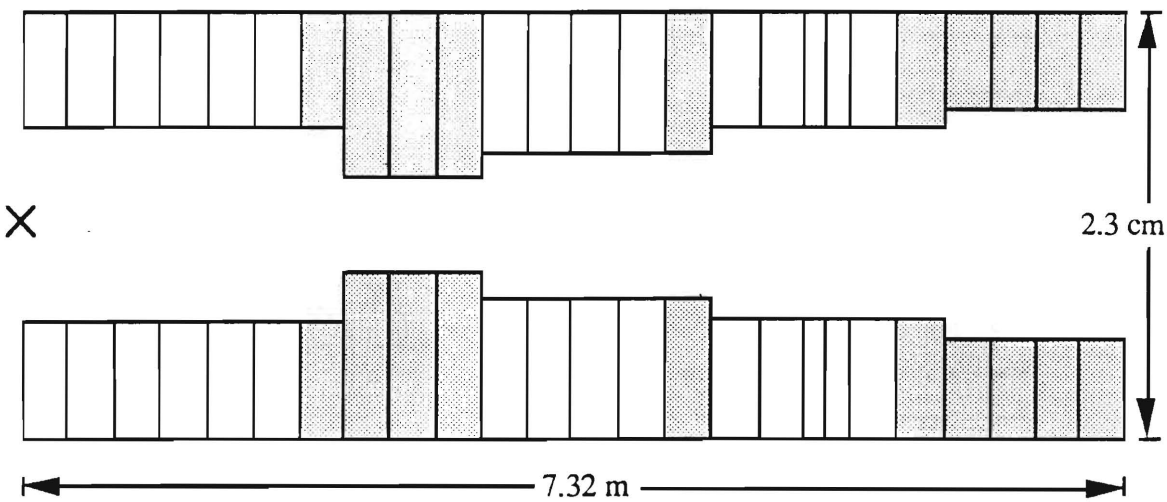

(b) Non - bend view

Brass

Tungsten

The center of the entrance of the collimator

Figure 2.4 (a) Bend view (b) Non-bend view (magnetic field of M1 perpendicular to this plane) of the collimator.

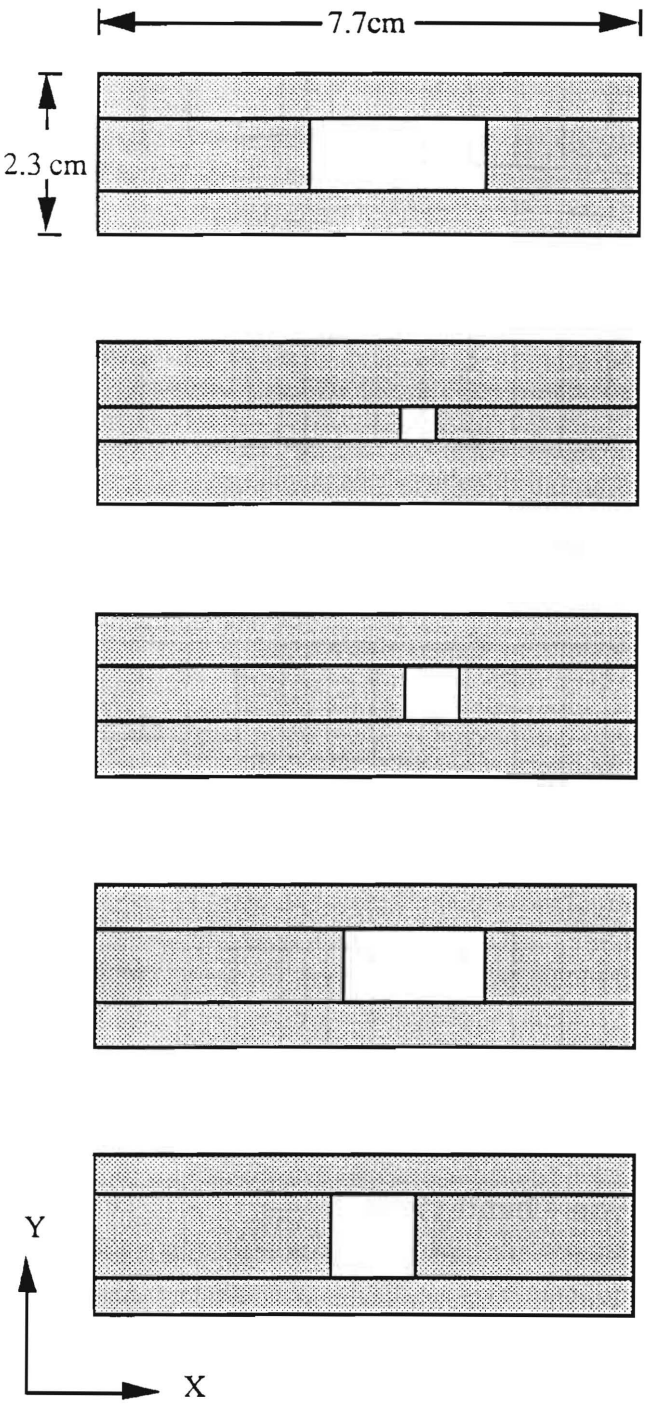

Distance from Entrance (m)	X Width (cm)	Y Width (cm)
2.13	2.54	1.02
3.05	0.50	0.50
4.57	0.76	0.76
6.10	2.00	1.01
7.32	1.22	1.22

Figure 2.5 Cross sections of the collimator.

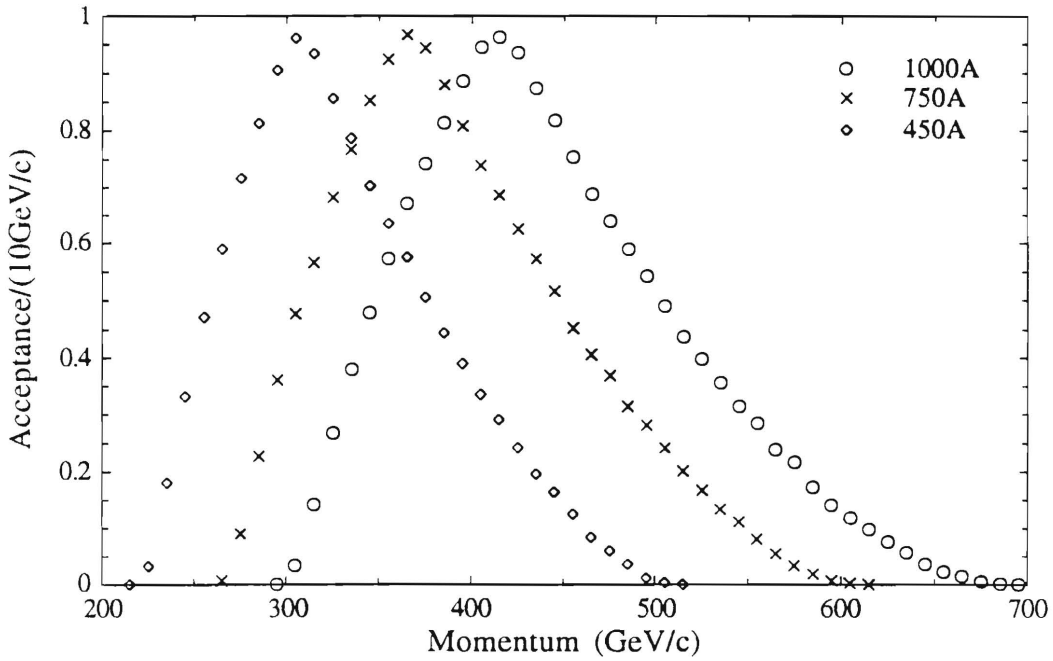

Figure 2.6 Channel acceptance of the collimator at different magnet currents.

The relative acceptance (defined as the fraction of charged particles that exits the channel after having cleared the defining collimator) of the channel as a function of momentum at the three magnet current values, or equivalently $\int Bdl$ values, as modeled with a monte-carlo simulation is shown in Figure 2.6.

2.3 Spectrometer

A plan view of the spectrometer is shown in Figure 2.7. Note in particular the coordinate system used. The positions and characteristics of the various detector elements are given in Table 2.2.

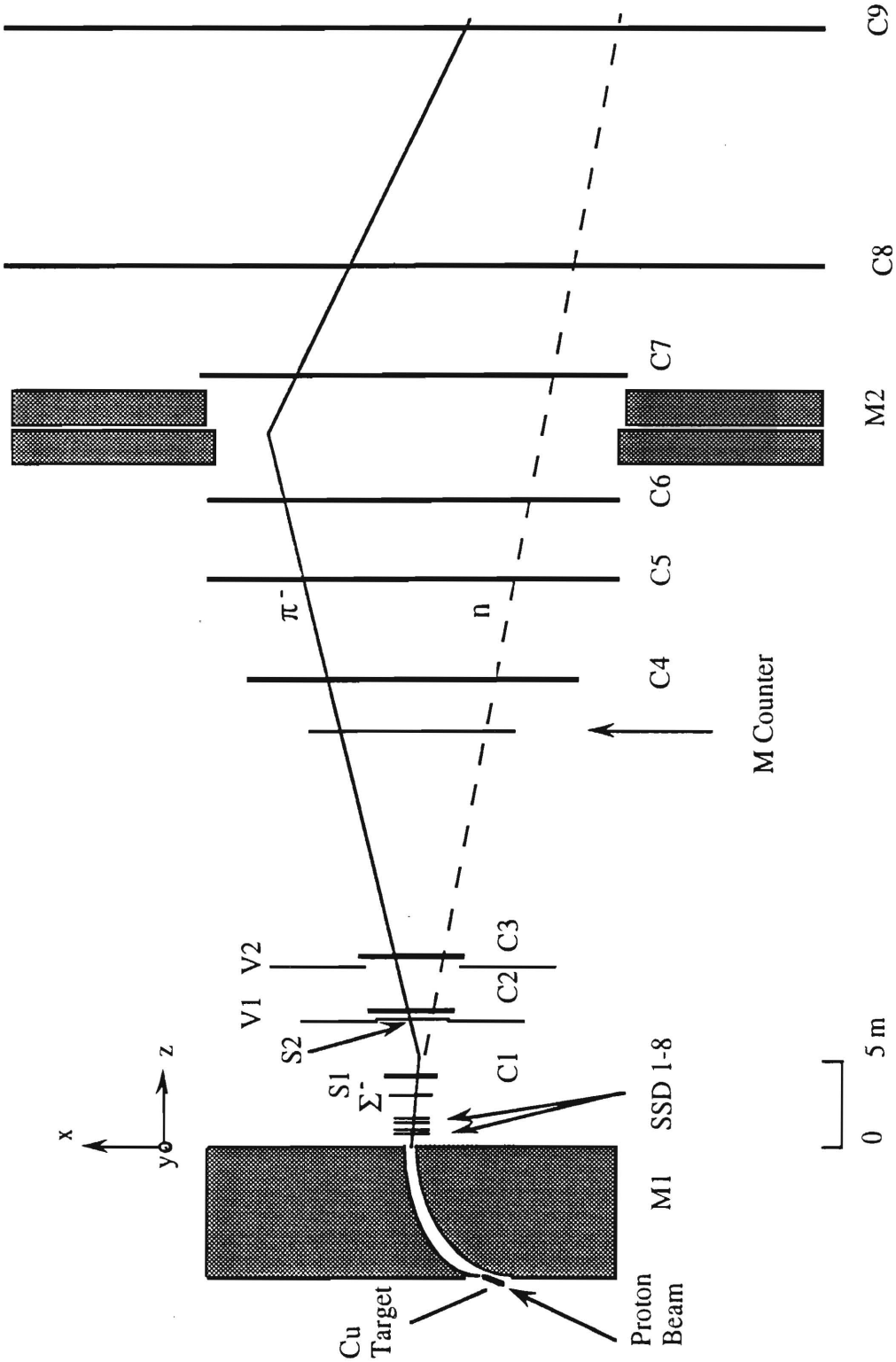

Figure 2.7 Plan view of the spectrometer. Note that the transverse dimensions have been exaggerated. (See Table 2.2)

(a) SSDs and Chambers

	Z (cm)	X × Y (cm^2)	Pitch (mm)
SSD 1X	86.2	2.8 × 2.8	0.1
SSD 1Y	94.5	2.8 × 2.8	0.1
SSD 2X	114.6	2.8 × 2.8	0.1
SSD 2Y	122.9	2.8 × 2.8	0.1
SSD 3X	143.0	2.8 × 2.8	0.1
SSD 3Y	151.3	2.8 × 2.8	0.1
SSD 4X	171.4	2.8 × 2.8	0.1
SSD 4Y	179.7	2.8 × 2.8	0.1
C1	405.5	12.8 × 12.8	1.0
C2	753.6	25.4 × 25.4	1.0
C3	1054.7	25.4 × 25.4	1.0
C4	2597.8	51.0 × 25.4	2.0
C5	3154.4	51.0 × 51.0	2.0
C6	3605.1	44.6 × 27.0	2.0
C7	4310.5	63.0 × 25.4	2.0
C8	4897.4	120.0 × 38.2	2.0
C9	6228.0	127.8 × 38.2	2.0

(b) Counters

	Z (cm)	X × Y (cm^2) (outside aperture)	X × Y (cm^2) (inside aperture)	Thickness (cm)
S1	369	6.4 × 3.8		0.1
S2	724	10.8 × 6.4		0.1
V1	723	32.4 × 8.9	10.8 × 6.4	0.3
V2	1014	41.9 × 11.4	14.0 × 8.3	0.3
M	2331	30.5 × 30.5		1.0

Table 2.2 (a) Z-position, aperture dimensions, and pitch of SSDs and multiwire chambers (b) Dimensions of scintillation counters. The chamber gas was 95% Argon, 5% Methylal, and 0.12% Freon by volume, operating at 2.7 to 4.2kV.

The charged particle beam was roughly defined by scintillation counters S1 and S2, and by V1 and V2 which vetoed beam halo. Counter M detected the charged multiplicity of an event (its pulse-height output was proportional to the number of charged particles).

The precise trajectories of the charged particles were determined by a set of eight silicon-strip detectors (SSD 1-8) with alternate detectors having their strips perpendicular to each other, and by nine multiwire proportional chambers (C 1-9) each of which had both a vertical and a horizontal signal plane (the exceptions were C4, whose two planes were rotated by ±45 degrees about the z-axis, and C5, which had an additional signal plane, called u-plane, also rotated by 45 degrees; these planes supplemented and correlated the x and y planes in the event reconstruction).

The momentum of the parent particle (the upstream track) was measured by magnet M1. This was possible since the production target and the defining collimator aperture provided two known points that defined the orbit of the parent particle through M1. The momentum of the daughter particle (the downstream track) was measured by magnet M2, which actually was made of two dipole magnets placed close (30cm) together. The analyzing magnet M2, whose field was known to about 1% accuracy, imparted a transverse momentum kick of 1.54 GeV/c to particles passing through it.

Helium-filled polyethylene bags were placed between the various elements of the detectors and inside M2 to minimize the effects of multiple coulomb scattering of the charged particles.

There were also a hodoscope array and stacks of lead-glass blocks arranged behind C9 that were meant for electromagnetic calorimetry and for detection of neutral particles. These were not used in this analysis, however.

2.4 Trigger logic and data acquisition

The experimental configuration was not specifically designed to detect the decay sequence of interest, $\Sigma^- \rightarrow n\pi^-$. In fact, the data acquisition system was optimized to trigger on three-track events such as $\Omega^- \rightarrow \Lambda K^-$, with $\Lambda \rightarrow p\pi^-$. However, a prescaled (scale factor being 64) single-track trigger was also implemented and mixed in with the three-track trigger. This trigger involved the coincidence of signals from scintillation counters S1 and S2 and the anti-coincidence of the halo vetos, V1 and V2. In symbols,

$$\pi = S1 \bullet S2 \bullet \overline{V1} \bullet \overline{V2}$$

Essentially, this triggered on all charged tracks--including those from the decay under study, $\Sigma^- \rightarrow n\pi^-$.

When this trigger is satisfied, a "busy" logic level was set to hold off further triggers. At the same time, an "enable" signal latched the hit data from the SSDs, MWPCs, as well as the signals from scintillation counters, and started the digitization process for various analog-to-digital (ADC) modules. Then an interrupt signal was sent to a PDP-11/45 computer to initiate the readout process, cumulating in the relevant data being written onto magnetic tape. At the end of this process, the busy level was removed and the latches reset, readying the system for another event. (Figure 2.8 shows the circuit block diagram for the MWPCs readout.) At the beginning and the end of each spill, an interrupt signal was also generated to enable the recording of ADC pedestals and gated and ungated scalers, including the single-track, three-track, and single-count rates in proportional chambers.

2.5 Calibration

The wire chambers and the silicon-strip detectors were aligned and surveyed in place perpendicular to the z axis and the z positions of the wire planes measured to

within 0.5 mm. The x and y positions of the centers of the planes were checked using single-track events with analysis magnet M2 turned off and a pencil beam of charged particles passed through M1 as follows. A straight line fit was made to all the hits except those of the given chamber. This gave a predicted value for the hit in that chamber. The difference between this value and the actual value was the residue. The correct center then was that which minimized the residues of a sample of straight-through single tracks. This gave values for the centers accurate to better than one tenth of the pitch of the detectors.

Using this method, it was also found that some chambers were slightly rotated about the z axis. Of these chambers, those that affected the tracking resolution were corrected in the reconstruction.

Since both the targeting of the beam and the field of M2 may vary with time, the effective target position and M2 field integral (M1 field is assumed to be accurately known from measurements with a Hall probe) were found using samples of beam tracks (non-decaying tracks of mostly pions) and reconstructed Σ^- tracks. This was done by tracing the beam tracks back to the target assuming a given value of M2. This gave sets of consistent target positions and M2 field integrals, which were then used to reconstruct the $\Sigma^- \rightarrow n\pi^-$ decays. The set that gave the correct Σ^- mass was then used in the analysis program.

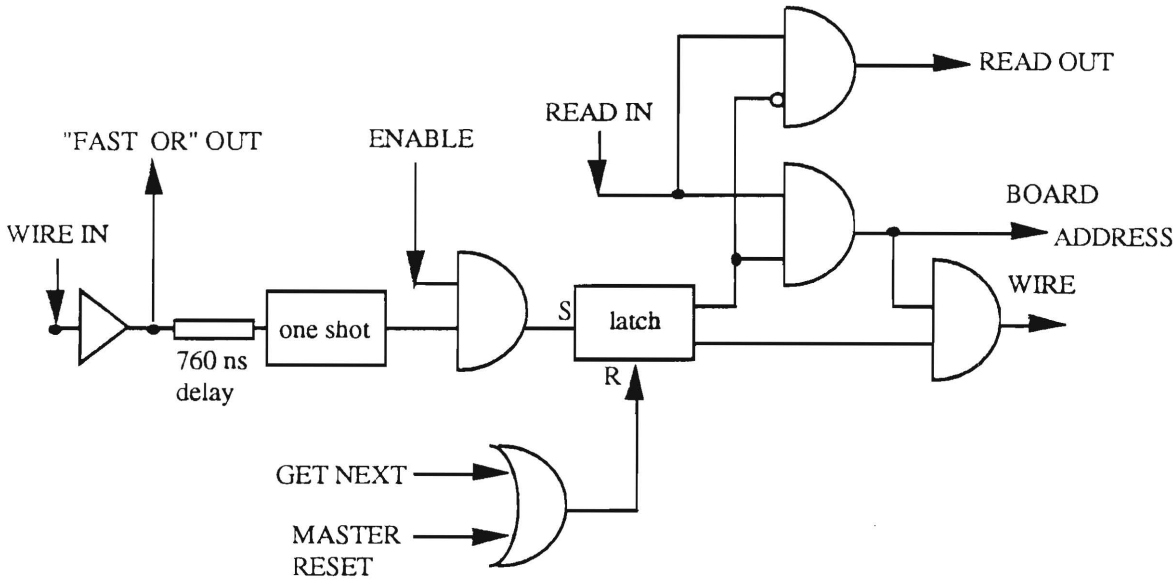

Figure 2.8 Block diagram for the readout circuit of a single MWPC channel. The raw signal from the wire hit is amplified, shaped, and delayed by ~760ns to allow a decision to made by the trigger logic (the "fast or" signal can be used as part of the trigger). If the trigger is satisfied, a busy signal is set to block further triggers; an "enable" pulse latches the wire hit; and an interrupt signal starts the readout process by a PDP11 computer. In this case, a serial "read-in" pulse that goes from board to board and chamber to chamber would stop at each hit wire and put its address on a bus directly to the computer. A "get next" pulse issued by the computer resets the latch and, at the same time, let the "read-in" continues propagating down the line (the "read-out" pulse).

CHAPTER 3

EVENT RECONSTRUCTION AND SELECTION

Analysis of the data, which consisted of recorded wire hits in each chamber plane and hits in the SSDs, proceeded first with the conversion of the hits into actual positions; then sorting and fitting these to the single-track decay topology (i.e., the topology of two track segments meeting at a kink, the "decay vertex", illustrated in Figure 3.1); and finally fitting the topology to the hypothesis, $\Sigma^- \rightarrow n\pi^-$. Data which were thus successfully reconstructed were next carefully selected to eliminate contaminations and backgrounds, and passed on to the polarization analysis program.

3.1 Event Reconstruction

The reconstruction of an event began with finding possible tracks through the set of hit points. The six downstream chambers (C4-C9) right before and after the analysis magnet were considered first in this tracking process. The single-track condition was minimally fulfilled by requiring at least two of the six chambers to have *single* hits in y, or non-bend, view. Spuriously reconstructed tracks were eliminated by requiring at least three hits in a straight-line fit in the y view. Physically

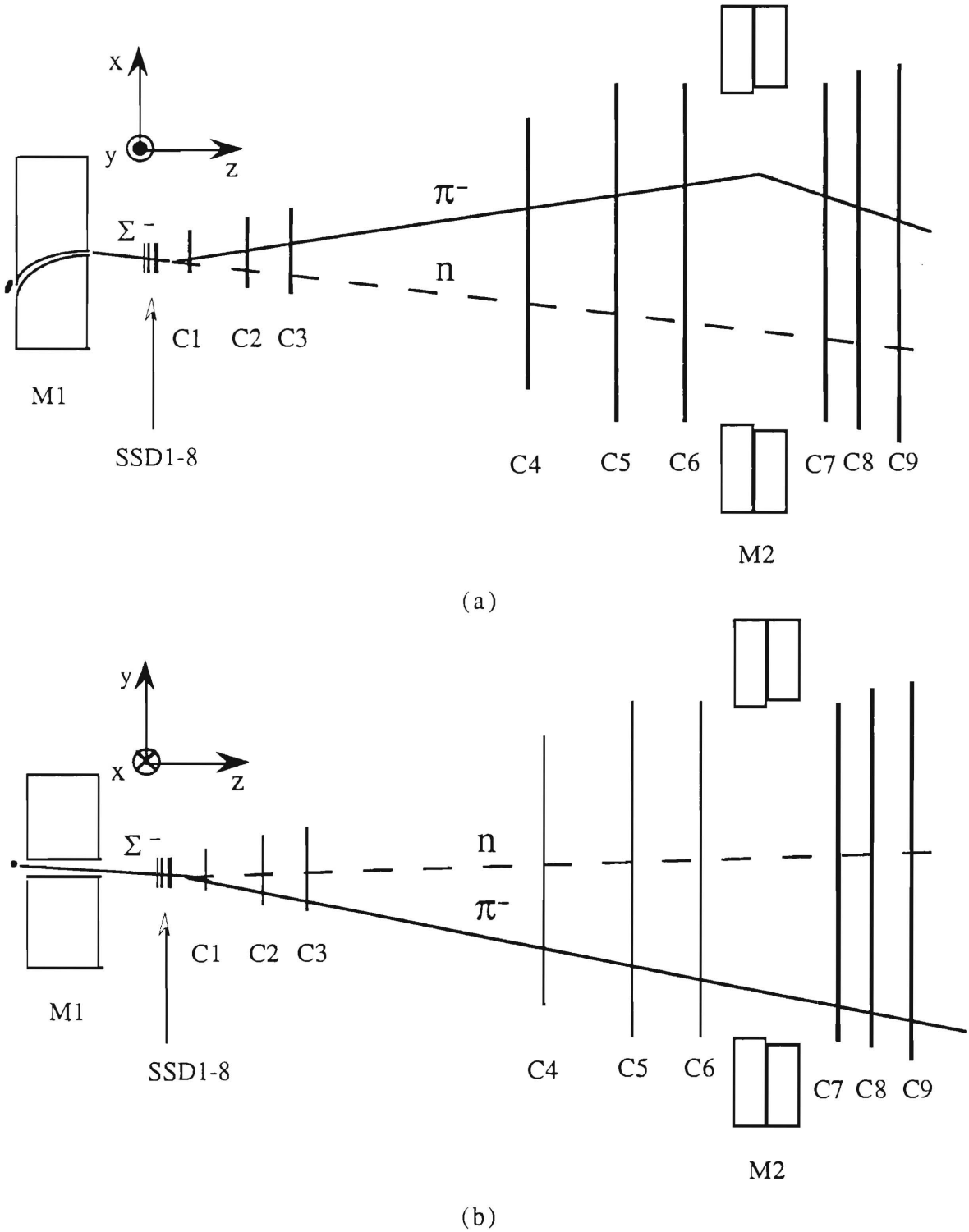

Figure 3.1 Single track topology for the case of the Σ^- (a)bend,(b) non-bend view

interesting tracks were found by insisting on the existence of two tracks that meet at the bend plane of the analysis magnet (M2) in the x, or bend, view.

Tracking continued next with the upstream chambers (C1-C3) and the SSDs. First, an attempt was made to see if the previously fitted track can be extended, in both views, to the upstream chambers using hits there. Thus, if adding an upstream hit close to the extrapolated track did not increase the χ^2 of the fit by more than five, then that hit was added to the fit. (χ^2 was defined as the sum of the squares of the residuals of each track at each detector plane divided by the corresponding resolution of the detector, where the residual of a track was the difference between the raw and the fitted positions.) This procedure tentatively defined the daughter track downstream of the decay vertex. Wrongly adding hits from the parent track upstream of the vertex to the daughter track would inordinately increase the χ^2 except in the case of very small opening angles.

Incidentally, at this juncture it might happen that the downstream track could be extended all the way to the aperture of the magnet M1 and then traced through the collimator back to the target with a perfectly reasonable χ^2 to boot. In this case, the track physically was a beam track consisting mostly of non-decaying pions. On the negative side, this sample of beam tracks was a nuisance that must be tested for and eliminated from the final data sample. On the positive side, this sample of beam pions could be used to check the previously found effective target and defining collimator positions, which were needed to define the parent track in the next step.

The parent track was found by assuming that the trajectory would start at the effective target position and would pass through the defining collimator and then extrapolating these two points, in the non-bend view, downstream to include closest hits in the SSDs and further chambers. For the procedure to work, of course, the first three SSD planes must have some hits at this stage. Again a hit would be added only if the χ^2 would not increase by more then five when it was incorporated into the fit. In the bend view, the target and defining collimator could not be used directly in the linear fit because in this view, the trajectory was no longer straight. However, if the various

possible tracks were linearly extrapolated backward from the exit aperture of the collimator, they all came to focus at a single point (see Figure 3.2). Thus, equivalently this virtual image "source" point (affectionately named Handler's node, after the ingenious experimenter who programmed this part of the reconstruction program) could be used to fit the parent track. It should be noted that the position of this virtual source was fixed by the positions of the target and defining collimator.

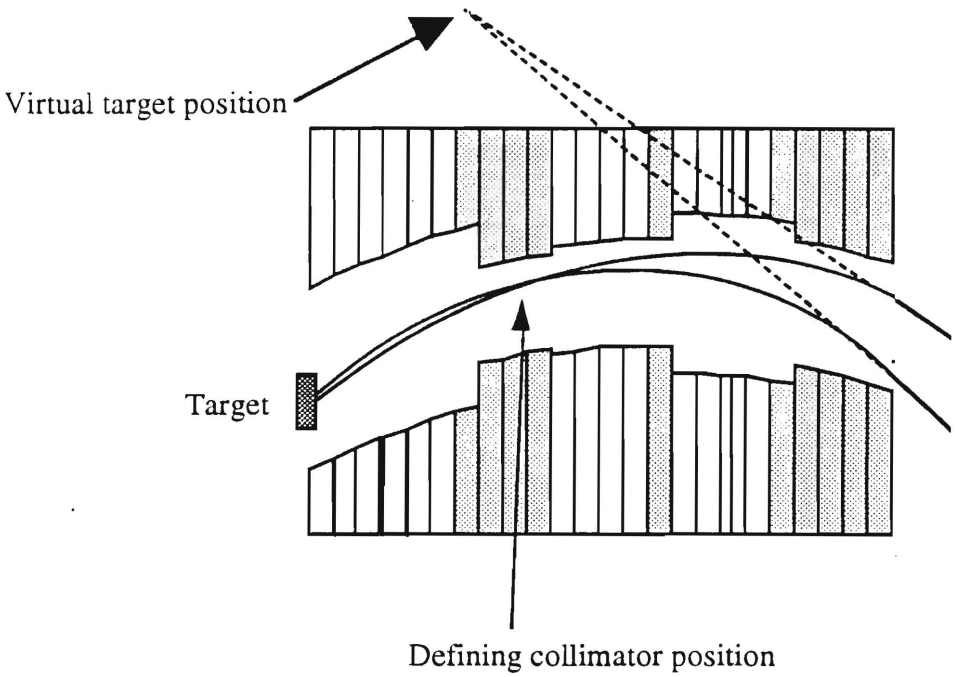

Figure 3.2 Virtual source point used in the bend-view reconstruction of the upstream track. Dimensions are greatly exaggerated for the sake of clarity.

Once the parent track and the daughter track were determined, the decay vertex could be fixed simply by their closest approach. However, this might be erroneous in the case of small opening angles when the union of the parent and daughter tracks differed very little from a single straight line. To ensure the correct determination of the vertex, an iterative procedure was used. The decay vertex was

alternately assumed to lie between the first pair and second pair of SSDs, between the second and third SSD pairs, etc. until lastly, between C3 and C4. In the first case, the first SSD pair would belong to the parent track while the rest of the SSDs and chambers would be part of the daughter track. The fit would be redone, its χ^2 recalculated, and the vertex redetermined under this assumption. After all the cases have been investigated in this way, the one with the smallest χ^2 gave the best estimate for the decay vertex position. Of course, some events fell short of this procedure either because there were not enough hits (at least three in x view) in the first few SSDs, or the iterative procedure failed to converge.

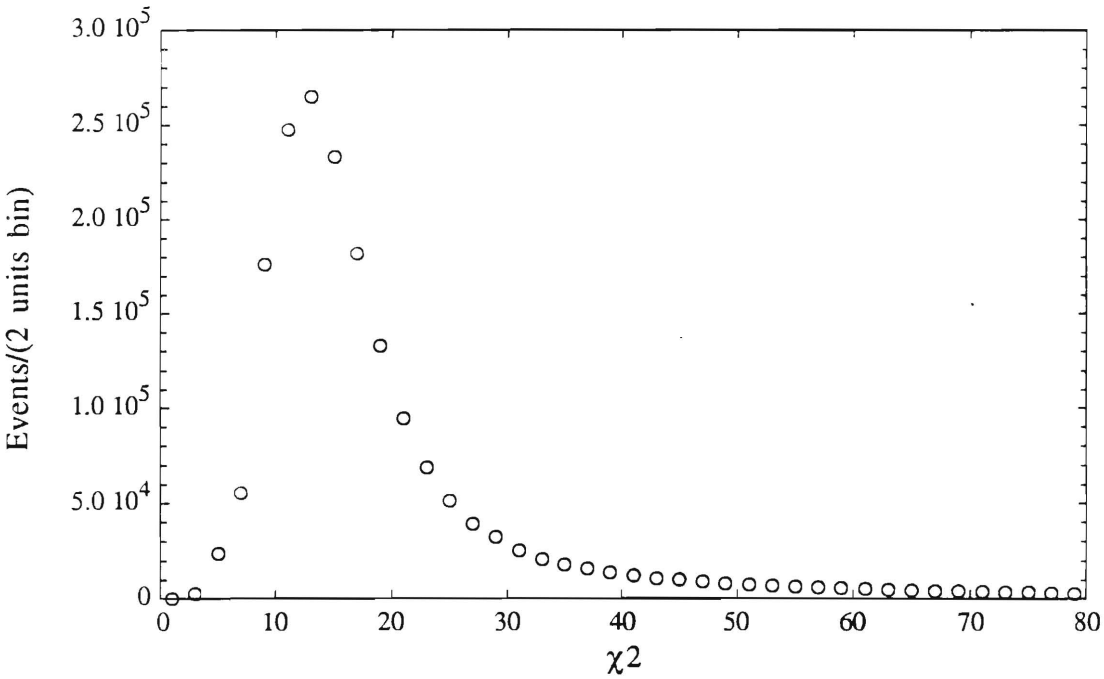

Figure 3.3 Distribution of geometric χ^2.

The distribution of χ^2 of the final geometric fit is shown in Figure 3.3. The overall geometric χ^2 was required to be less than 80 for 15 degrees of freedom typically. Events with χ^2 larger than this were cut from the data sample. There was also an implicit fiducial region cut. This was because the decay vertex was required to

be between the first SSD pair and C4. A summary of the different event failure/success classes in the reconstruction program is give in Table 3.1. The table also gives percentages of the original data sample that were discarded up to this point (classes 1 to 6). Approximately 77% of the events (class 0) were properly reconstructed single-track events.

Class	%	Description
1	9.5	Less than 2 chambers (among the 6 downstream chambers) with single hits in y-view
2	3.5	Less than 3 points in straight line fit in y-view in the 6 downstream chambers
3	1.0	No bend at M2 in x-view
4	0.5	No hit found in first 3 SSD planes
5	7.0	Geometric $\chi^2 > 80$
6	1.5	Could not find a kink by iteration
0	77.0	1- track candidate.

Table 3.1 Description of different classes of events in the reconstruction program. The percentages give the number of original data sample belonging to each class

At the end of the geometric fit, momenta of the upstream and downstream tracks could be calculated. The downstream momenta came from a knowledge of the track bend and the field of the analysis magnet; the upstream, from the track-fitting of the target and defining collimator points to the upstream chambers and the field of the hyperon magnet.

A kinematic fit of the raw hit data was also performed where the hypothesis $\Sigma^- \rightarrow n\pi^-$ was assumed from the very beginning (i.e. the masses were all known, including the Σ^- mass). However, no information from this fit was used in the final analysis. The difference in the χ^2 of this fit and the geometric χ^2 is the so-called kinematic χ^2, and is shown in Figure 3.4 for a typical run.

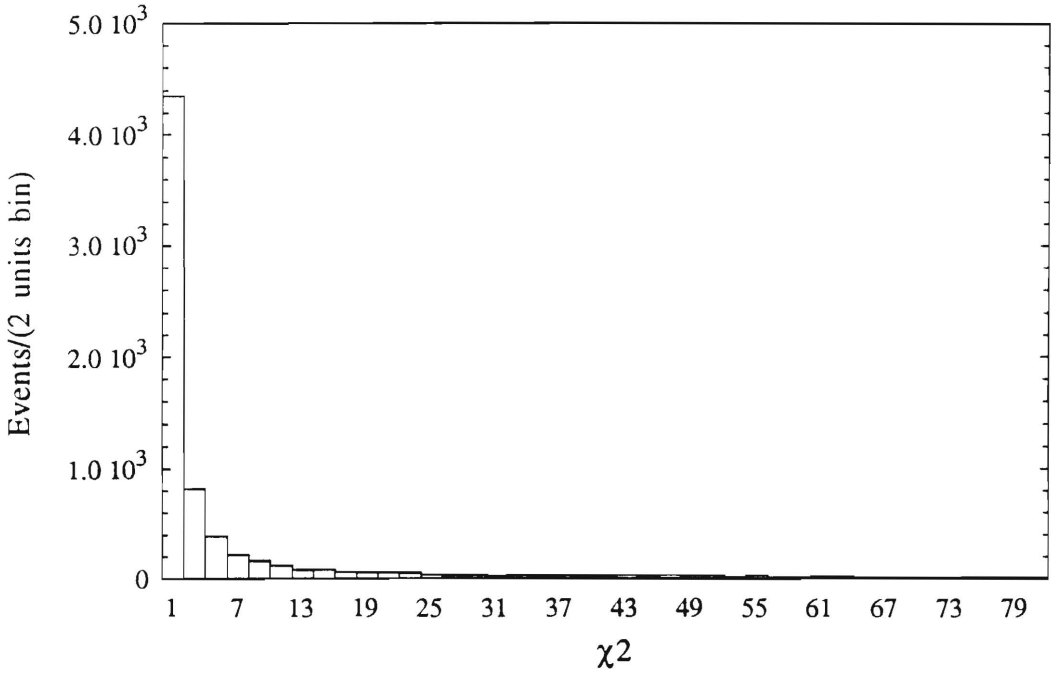

Figure 3.4 Distribution of kinematic χ^2 for a typical run.

At the end of this process, the reconstructed information--namely, the parent and daughter momenta, decay vertex, and χ^2 values--were written out to data summary tapes for further selection and analysis.

3.2 Event Selection

To glean from the data summary tapes the events of interest, $\Sigma^- \rightarrow n\pi^-$, further work was necessary to clean up the sample and to eliminate background events of the same single-track topology such as the following:

$\Xi^- \rightarrow \Lambda + \pi^-$, followed by $\Lambda \rightarrow n + \pi^0$

$K^- \rightarrow \pi^0 + \pi^-$

$\overline{\Sigma}^- \rightarrow n + \pi^-$

$\overline{\Sigma}^- \rightarrow \pi^0 + \overline{p}$

$\Omega^- \rightarrow \Lambda + K^-$

To do this, the data was visualized in terms of distributions of various physical parameters. A monte-carlo simulation of the experiment (apparatus and physics) gave an indication of what these distributions should look like ideally for the decay under study, $\Sigma^- \rightarrow n\pi^-$. Based on comparisons with the monte-carlo, a series of cuts could then be applied to the data to select only the desired events.

A digression should be made here to the effect that not too much importance should be placed on the monte-carlo. It was useful as a tool to study the possible effects of the physical configurations of the apparatus--such things as the dimension and resolution of the chambers--on the physics. But, in the final analysis, it was only a guide--and a rough one at that--to the physics contained in the real data, even though efforts were made to incorporate certain features of the real data into the monte-carlo (for example, the production momentum spectrum of the parent particle was matched to that from the real data). The reason is that the real data might be polarized by an unknown amount. And this polarization has an observable effect on the various distributions. The solution to this is to use the so-called hybrid monte-carlo described in the next chapter.

Meanwhile, an outline of the basis for the cuts applied to the real data follows. For simplicity, arguments will be made explicit only for the data sample taken at a

sweeper current of -450A and negative production angle (c.f. Table 2.1); but they carry over analogously for the samples at the other running conditions (namely -750A, and -1000A at ± production angles).

1) Geometric χ^2 cut

This was one of the more important "clean up" cuts as it affected the overall quality of the sample of single-track data. Events that failed this cut were those whose claim to having the proper topology is highly suspect--mainly no-kink or straight-through beam tracks, consisting mostly of non-decaying pions.

A loose geometric χ^2 cut of 80 was previously imposed. The χ^2 distribution of the data sample at this point is shown in Figure 3.3. Typically there were 23 data points and eight parameters (slopes and intercepts of the upstream and downstream tracks), giving 15 degrees of freedom for these fits. A cut on χ^2's larger than 45 was now additionally applied. Monte-carlo simulation indicated that less than 1% of the real Σ^- events would be lost by this cut.

2) Momentum cut

Figure 3.5 shows the distribution of the Σ^- momentum. Monte-carlo modeling of the channel indicated that its momentum acceptance range was about 215-515 GeV/c (see Figure 2.5). In fact, the acceptance was small below 240 GeV/c, and events with parent (upstream track) momenta below this value were cut. Similarly events with Σ^- momenta above 500 GeV/c were also cut.

3) Decay vertex cut

As mentioned previously, the reconstruction routines made an implicit fiducial cut that excluded events whose z positions of the decay vertex fell outside the region between the first SSD pair and chamber C4, that is between approximately 85 cm and 2600 cm. At the present stage, a slightly more restrictive, explicit cut was made. Events with z positions upstream of 150 cm

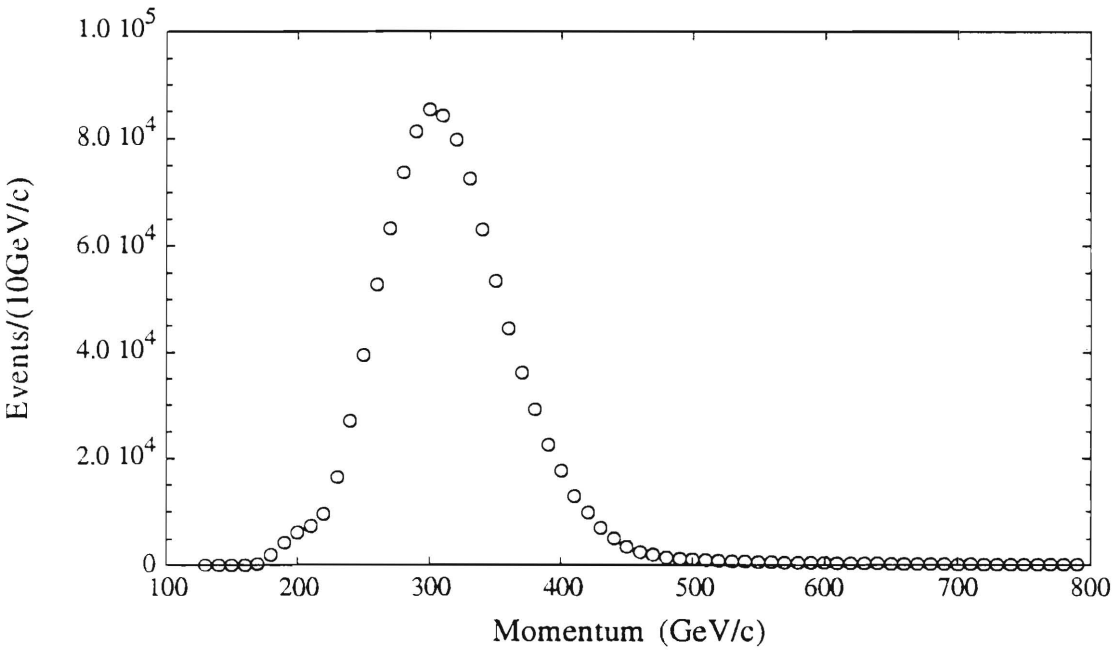

Figure 3.5 Distribution of the parent's (upstream track's) momentum after χ^2 cut for -450A sample at negative production angle.

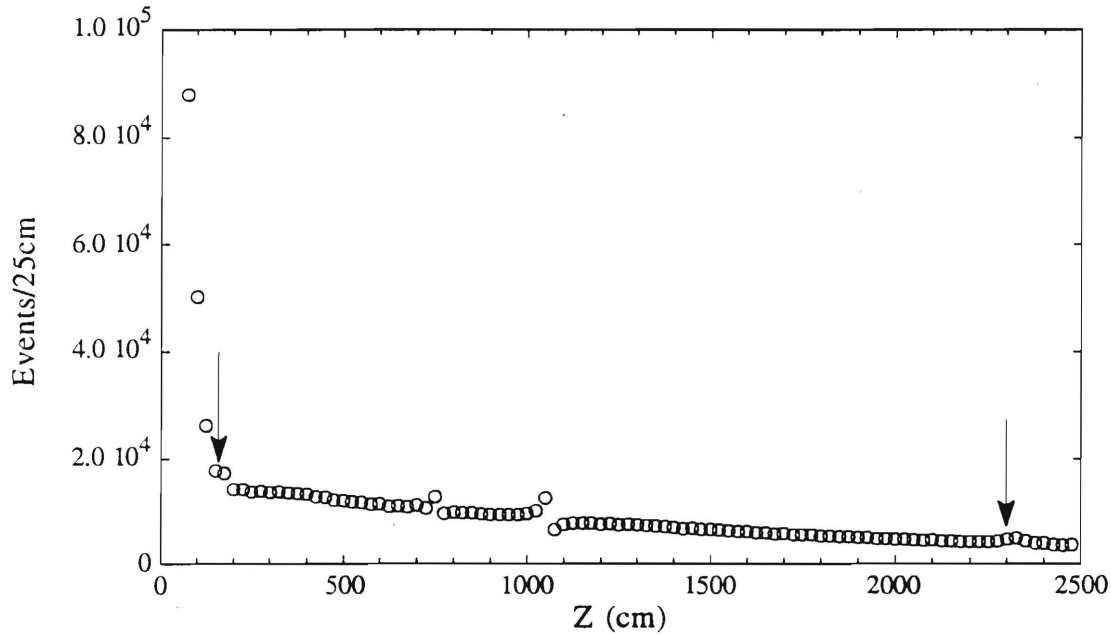

Figure 3.6 Distribution of the z position of the decay vertex after χ^2 and momentum cuts for -450A sample at negative production angle.

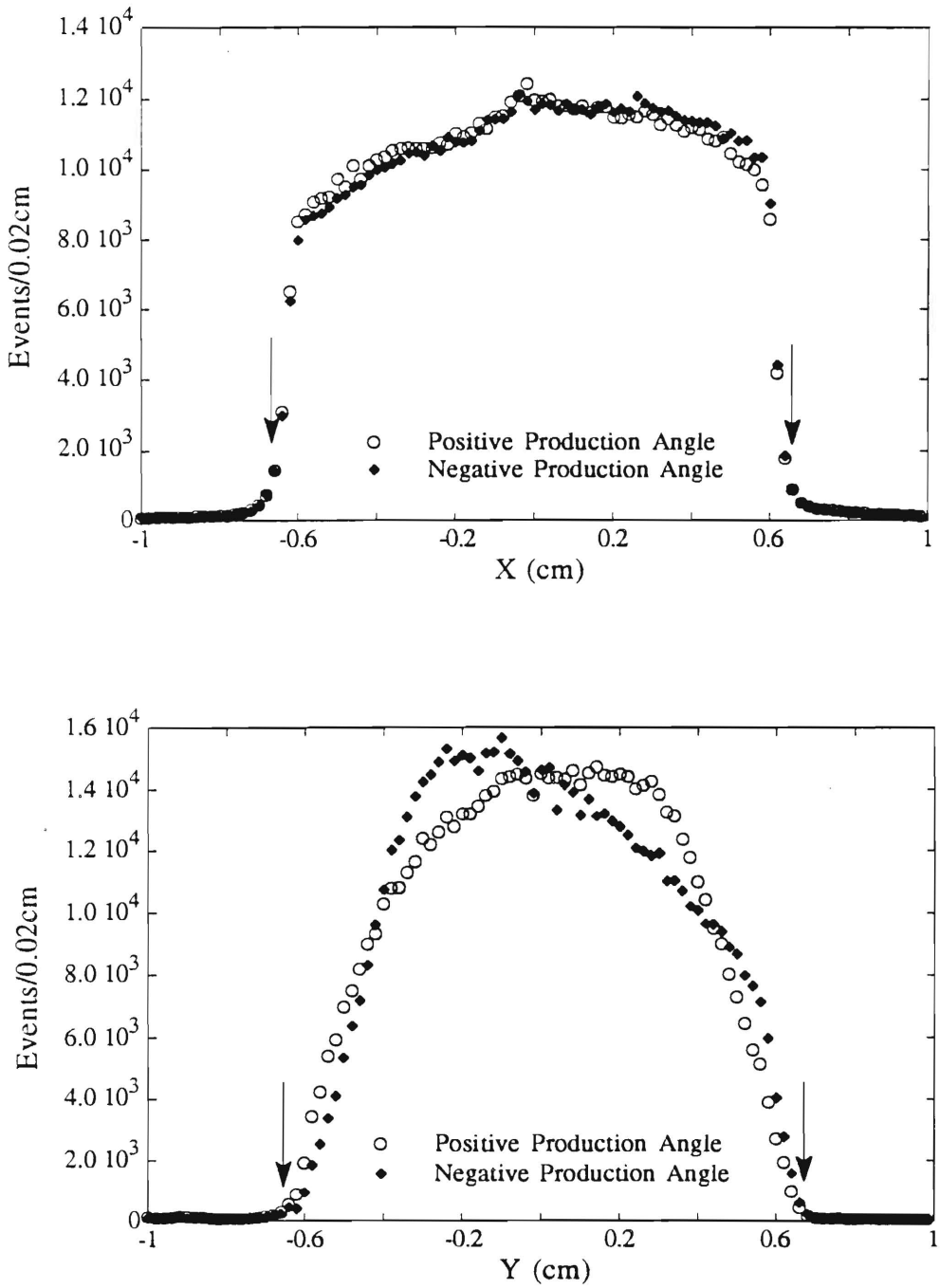

Figure 3.7 Projections of the upstream track at the exit aperture of the hyperon magnet for -450A sample. Data for the negative production angle was normalized to that of positive production angle.

and downstream of 2300 cm were cut. The latter bound was just enough to put the M counter (at 2331 cm) outside of the fiducial region. (In the analysis of three-track events, the M counter was found to be a source due to the interaction of beam particles with the scintillator material; a perceptible bump can be seen at the M counter position in Figure 3.6.)

4) Exit aperture cut

When the upstream track was traced back to the exit aperture of the hyperon magnet from the decay vertex, the resultant projections are as shown in Figure 3.7. Since the physical aperture was a 1.22 x 1.22 cm^2 square, cuts were made (at the arrows in the figure) to reflect this fact. These cuts are similar to a target pointing cut in that they reject events that were most probably produced inside the collimator.

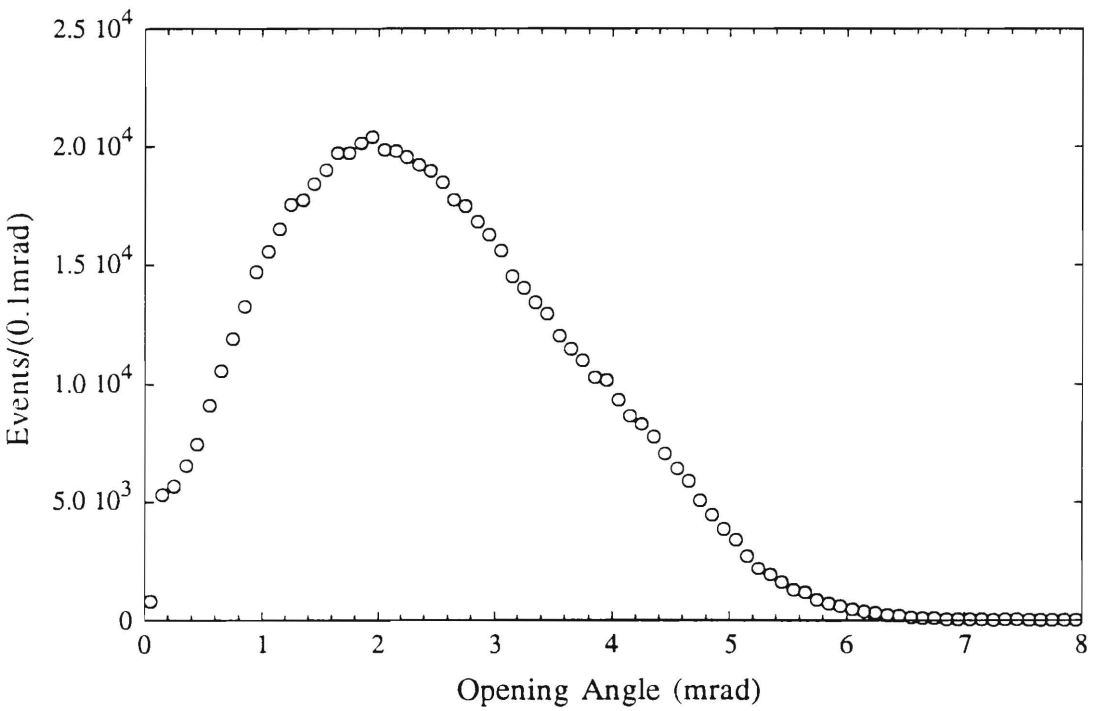

Figure 3.8 Distribution of Σ^--π^- opening angle for -450A sample at negative production angle.

In the figure, data for both production angles are shown. The two sets of data match well along the x view, but differ significantly in the y view. This reflects the facts of vertical targeting: for the positive production angle case, the beam is going up in the +y direction while for the negative production angle, it is going down in the -y direction; all the while remaining centered in the x direction. (recall Figure 1.1). This artificial asymmetry in the beam distribution gives rise to a false y asymmetry, as will be discussed in Chapters 4 and 5.

5) Opening angle ("kink angle") cut

A cut was made to exclude events with Σ^--π^- opening angles less than 0.16 mrad--essentially the first two bins of Figure 3.8; this eliminated possibly wrongly reconstructed straight (π^-) tracks.

6) Σ^- mass cut

All the cuts so far have made no assumptions involving the decay of interest, $\Sigma^- \rightarrow n\pi^-$. They were rather general cuts based on geometrical constraints of the hardware and software of the experiment and were designed to improve the quality of the whole sample of single-track events.

The hypothesis is now made that the daughter particles were indeed a neutron and a pion--i.e. that the decay was of the form $X \rightarrow n\pi^-$. The invariant mass of the parent particle, m_X, could then be calculated from the measured three-momenta of the upstream and downstream tracks (p_X and p_π). The resultant distribution is shown in Figure 3.9. The slight slope to the left of 1.175 GeV/c^2 indicates presence of background events. Monte-carlo simulations indicate that Ξ^-s wrongly reconstructed as Σ^-s will populate this region of the spectrum and, further, that such background drops off sharply to a negligible level at a distance of about 5 σ (at 1.175 GeV/c^2) from the Σ^- peak (Figure 3.10). To obtain a background-free sample of Σ^- then, the invariant mass was required to be within $\pm 5\ \sigma$ of the mass of the Σ^- (1.197 GeV/c^2).

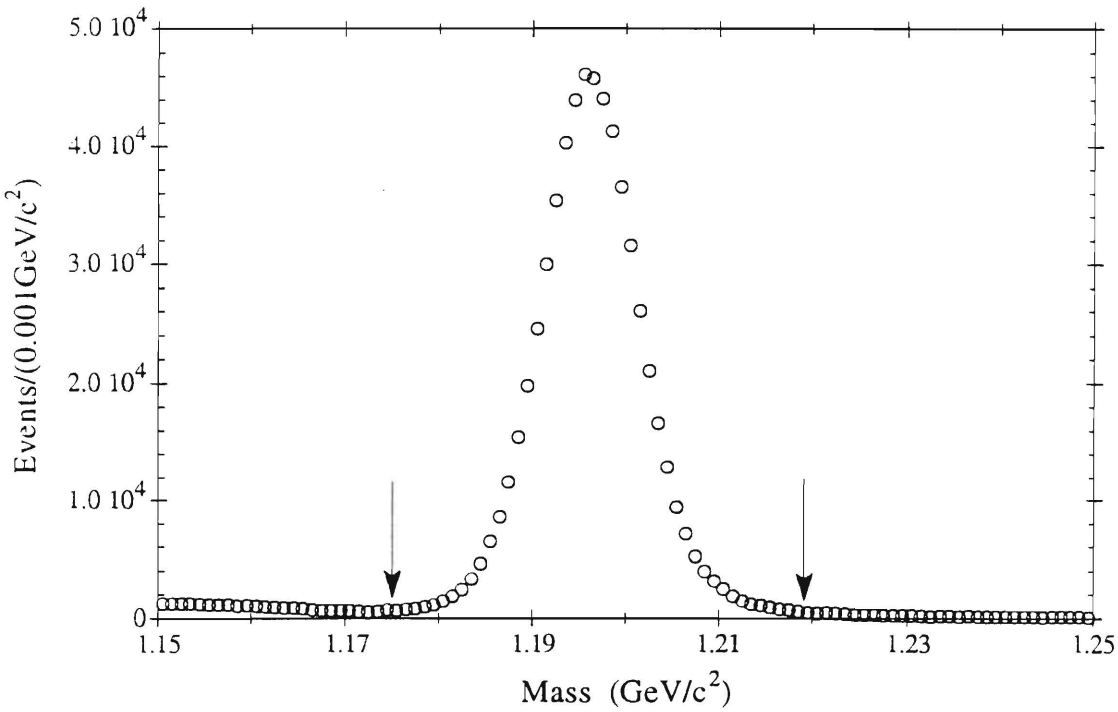

Figure 3.9 Candidate Σ^- events (reconstructed under the hypothesis $\Sigma^- \rightarrow n\pi^-$) after all but the mass cut for -450A sample at negative production angle. The slight slope to the left is due to a cascade background ($\Xi^- \rightarrow \Lambda\pi^-$). Cuts will be made at the places pointed to by the arrows.

These then were all the cuts applied to the data sample at -450A to cull out the desired Σ^- events. Similar cuts based on analogous considerations were applied to the -750A and -1000A samples. Table 3.2 is a summary of the typical percentages of events discarded by the various cuts; Table 3.3 displays the final distribution of events among the various running conditions.

The cuts were all rather "soft" and generously loose. This is fortunate for the subsequent polarization analysis is quite sensitive to cuts. Hard cuts will distort the distributions of direction cosines of the daughter particles, which carry the polarization signal. Not only that, hard cuts will also decrease the effectiveness of the hybrid

monte-carlo method which depends for its operation on the ability of monte-carlo events to probe all of the theoretically available phase space.

Cut	%
Geometric χ^2	5.1%
Momentum	5.4%
Decay Vertex	22.5%
Exit Aperture	1.7%
Opening Angle	1.0%
Σ^- Mass	7.5%

Table 3.2 Typical distribution of percentage of events cut out by the different event-selection cuts.

Sweeper Current (A)	Sweeper $\int$Bdl (T·m)	Production Angle Positive	Production Angle Negative
-450	-14.48	553,083	585,454
-750	-17.88	15,197	15,627
-1000	-19.44	75,348	59,901

Table 3.3 The final distribution of events under various running conditions.

Soft though they were, these cuts were effective in suppressing most sources of background. That this is so is dramatically exhibited in the distribution of the missing mass (i.e. the neutral daughter particle). Figure 3.11a shows the missing mass distribution when the charged daughter was assumed to be a π^- and the parent, a Ξ^-. Evidently there is a clear peak at the mass of the Λ (1.116 GeV/c^2), signaling

the definite presence of the first--and dominant--source of background listed at the beginning of this section, namely, $\Xi^- \rightarrow \Lambda\pi^-$. Figure 3.11b shows the same distribution after all the cuts have been applied. Obviously, the Ξ^- background has been eliminated. The monte-carlo showed that the cuts were 98% effective in removing Ξ^- events. Thus the cuts reduced the estimated fraction of Ξ^- from about 10.5% in the uncut sample down to a negligible 0.21%.

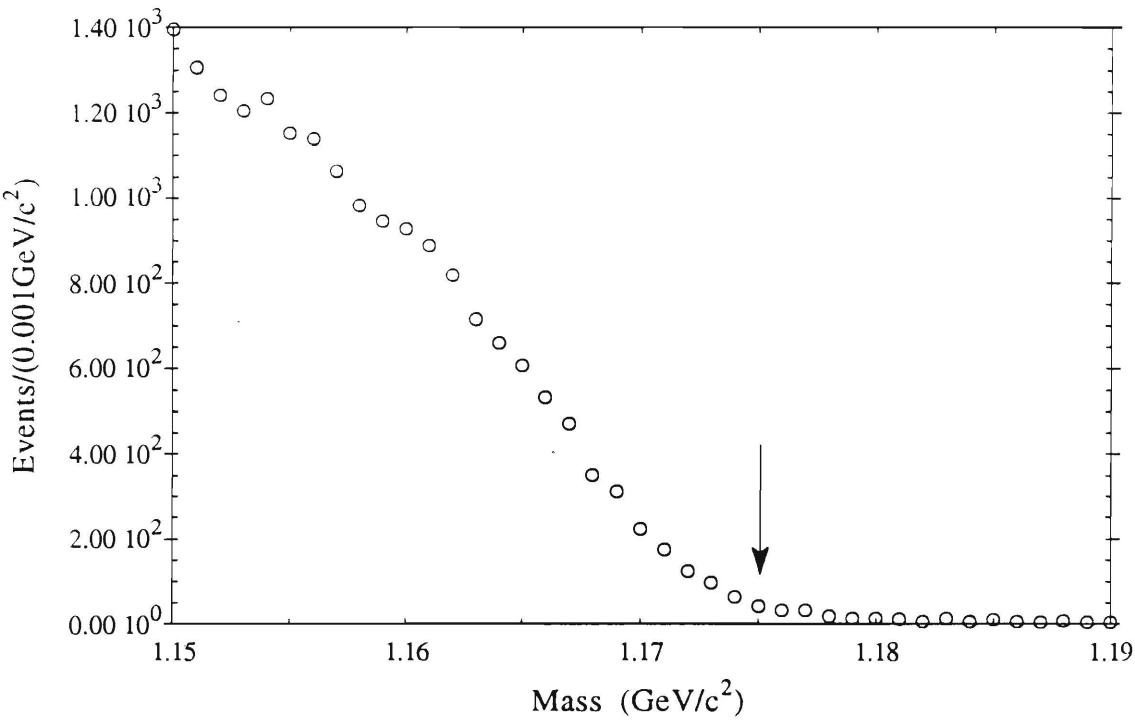

Figure 3.10 Monte-carlo $\Xi^- \rightarrow \Lambda\pi^-$ events reconstructed as $\Sigma^- \rightarrow n\pi^-$ events show a sharp drop off at a distance $\approx 5\ \sigma$ (at the arrow) from the Σ^- mass peak. The number of Ξ^- events in this graph has been normalized to 10.5% of the number of real Σ^- events for the negative production angle (the majority of Ξ^- events falls outside the lower end of the graph).

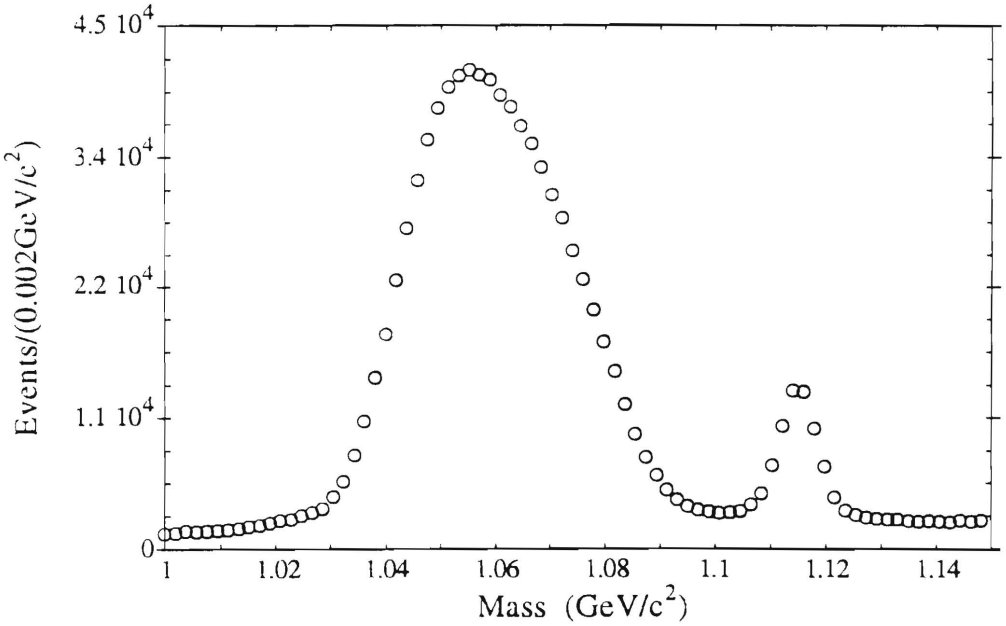

(a)

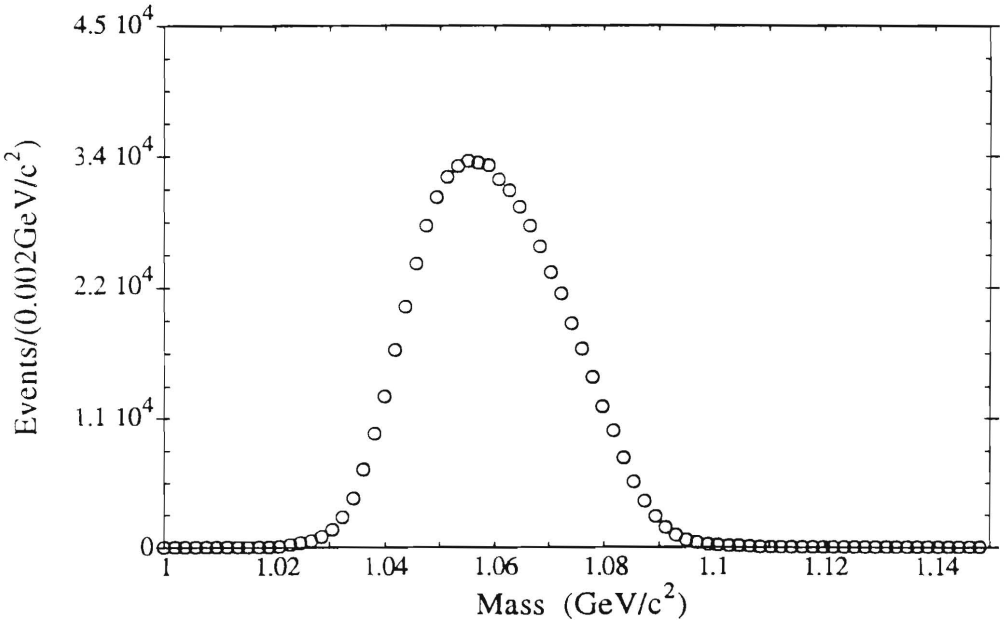

(b)

Figure 3.11 Missing mass distribution with the charged daughter assumed to be a $\pi^-$and the parent to be a Ξ^- , (a) before all cuts, (b) after all cuts for 450A sample at negative production angle. Note the lambda peak at 1.116 GeV/c2 in (a).

Things are even better for the hypothesized background source, $K^- \rightarrow \pi^0\pi^-$: apparently, there are none. This is attested to by the smooth missing mass distribution of Figure 3.12; no evidence of a π^0 peak can be seen. Moreover, the K^- background can have no polarization (spin 0 particle) and, therefore, can enter the measured asymmetry only through acceptance effects.

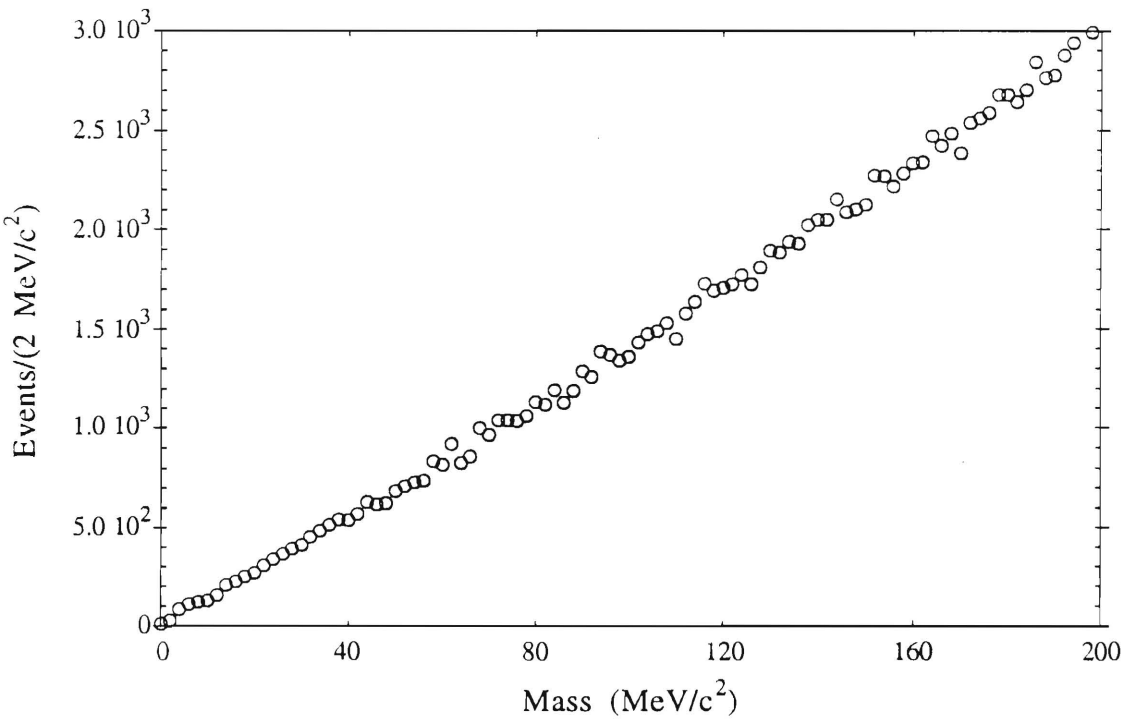

Figure 3.12 Missing mass distribution, before any cuts, with the charged daughter assumed to be a π^- and the parent, a K^-. No apparent π^0 peak (at 135 MeV/c^2)can be seen.

Of the three remaining sources of background cited at the beginning of this section, the $\Omega^- \rightarrow \Lambda K^-$ source is quite negligible. The experimental apparatus has very low acceptance for $\bar{\Sigma}^- \rightarrow \pi^0\bar{p}$ with its stiff $\bar{p}$. The only questionable source that remains is the $\bar{\Sigma}^- \rightarrow \bar{n}\,\pi^-$. Since the final state particles of this decay are indistinguishable from those of the decay of interest, $\Sigma^- \rightarrow n\pi^-$, the only way to

separate the two is via the meager 8 Mev mass difference between the parent particles. Fitting two mass distributions separated by this amount to the experimental data gives an estimate for the contamination from this source of a few percent, resulting in a change in the measured Σ^- polarization of the order $\leq 0.5\%$.

CHAPTER 4

POLARIZATION ANALYSIS

4.1 Introduction

In this experiment, the polarization of the Σ^- was measured by observing the angular dependence of its decay distribution. To see how, a more detailed look at the decay is in order.

For the principal (branching ratio $\approx$ 1) decay mode, $\Sigma^- \rightarrow n\pi^-$, the initial state has a total angular momentum of 1/2. Conservation of momentum then allows the final-state n-π system to have an orbital angular momentum of either 0 or 1, as the spin angular momentum of the π^- is 0 and the neutron 1/2. In fact, the final state is a linear combination of both orbital states. This is allowed as the decay is weak and therefore not required to conserve parity: the "s state" (angular momentum, L=0) and the "p state" (L=1) have inequivalent parity values whereas the intial Σ^- state has definite parity.

Let S and P be the amplitudes of the s and p states, $|s\rangle$ and $|p\rangle$, respectively. The final state can be written as

$$|f\rangle = S|s\rangle + P|p\rangle \tag{4.1}$$

For the case where the Σ^- has its spin up, the initial state $|i\rangle = |J=1/2, J_z=1/2\rangle$, so conservation of angular momentum for **J=L+S** dictates that

$$\begin{aligned} |s\rangle &\propto Y_0^0 \uparrow \\ |p\rangle &\propto \sqrt{\frac{1}{3}} Y_1^0 \uparrow - \sqrt{\frac{2}{3}} Y_1^1 \downarrow \end{aligned} \tag{4.2}$$

where use has been made of notations and results from atomic physics with $Y_l^m(\theta,\phi)$ being the standard spherical harmonic functions and the up and down arrows being shorthand for the spin states of the neutron. So then the angular decay distribution of the final-state neutron in the Σ^- rest frame is

$$\begin{aligned} \frac{dN}{d\Omega} &\propto |\langle f | f\rangle|^2 \\ &\propto \left| S \cdot Y_0^0 \uparrow + P \cdot \left(\sqrt{\frac{1}{3}} Y_1^0 \uparrow - \sqrt{\frac{2}{3}} Y_1^1 \downarrow \right) \right|^2 \end{aligned} \tag{4.3}$$

Working out this transition matrix gives

$$\frac{dN}{d\Omega} \propto 1 + \alpha \cdot \cos\theta \tag{4.4}$$

where θ is defined with respect to the direction of the Σ^- spin and

$$\alpha = 2 \cdot \frac{\mathbf{Re}\left(S^* P\right)}{\left(|S|^2 + |P|^2 \right)} \tag{4.5}$$

And, similarly, for the case with the Σ^- spin down ($| i \rangle = | 1/2,-1/2 \rangle$),

$$\frac{dN}{d\Omega} \propto 1 - \alpha \cdot \cos\theta \tag{4.6}$$

The analyzing power, α, characterizes the decay of the Σ^- and is rather small, $\alpha \approx 0.068$.[21] (As a digression, note that if the angular decay distribution of the final-state π^- instead of neutron is under consideration, $\alpha \approx -0.068$, i.e. $\alpha_{\pi^-} = -\alpha_n$.) This fact makes a measurement of the asymmetry of the $\Sigma^- \rightarrow n\pi^-$ decay distribution much harder than that of, say, the decay $\Sigma^+ \rightarrow p\pi^0$ which has an almost maximal α of ≈ 0.979.

The initial state of an ensemble of decaying Σ^-, such as a particle beam, is a statistical mixture of Σ spin-up states and Σ spin-down states:

$$| i \rangle = \frac{N^+ | 1/2,1/2 \rangle + N^- | 1/2,-1/2 \rangle}{N^+ + N^-} \tag{4.7}$$

where $N^{+(-)}$=number of Σ^- with spin up (down). This will give rise to the angular decay distribution

$$\frac{dN}{d\Omega} \propto N^+(1 + \alpha\cos\theta) + N^-(1 - \alpha\cos\theta) \tag{4.8}$$

If $N^+ = N^-$ then the Σ^-'s are unpolarized and the distribution is independent of $\cos\theta$. In general, however, N^+ and N^- will not be the same. The ensemble is then said to have a net polarization along the quantization axis--i.e. it has the polarization vector

$$\mathbf{P} = \frac{N^+ - N^-}{N^+ + N^-}\mathbf{n} \tag{4.9}$$

where n is the unit vector along the quantization axis. In terms of **P** the decay angular distribution is

$$\frac{dn}{d\Omega} = \frac{1}{4\pi}(1 + \alpha \mathbf{P} \cdot \mathbf{q}) \tag{4.10}$$

where **q** is the unit vector along the neutron direction of flight, $n = (N^{+}-N^{-})/(N^{+}+N^{-})$, and a normalization factor of $1/4\pi$ has been put in explicitly. Essentially, the expression says that the neutron will more likely be emitted in the direction of the Σ^{-} polarization than in the opposite direction--i.e. the decay distribution exhibits an asymmetry. Integrating the expression over the azimuthal angle gives

$$\frac{dn}{d(\cos\theta)} = \frac{1}{2}(1 + \alpha \mathbf{P} \cdot \mathbf{m} \cos\theta) \tag{4.11}$$

where **m** is any arbitrary unit vector and θ is the direction cosine of the neutron with respect to **m**. In this experiment, by picking **m** to be alternately the unit vectors **x**,**y**,**z** in the Σ^{-} rest frame that are parallel to the corresponding laboratory axes, the components of the polarization vector **P** could be measured.

4.2 Method

4.2.1 Graphical Method

From the result of the last section, if Σ^{-} events were histogramed according to their direction $\cos\theta_j$ for any given direction j, the number of events per $\cos\theta$ bin would be given by

$$\Delta N_j \propto \left(1 + \alpha P_j \cos\theta_j \right) \Delta(\cos\theta_j) \tag{4.12}$$

i.e. the distribution would be linear (see Figure 4.1) with a slope proportional to αP_j.

Actually, because the experimental apparatus had a finite acceptance and resolution, this distribution should be modified to

$$\Delta N_j^{\pm} = \frac{1}{2} A_j^{\pm}(\cos\theta)\left(1 + \alpha P_j \cos\theta_j\right)\Delta(\cos\theta_j) \tag{4.13}$$

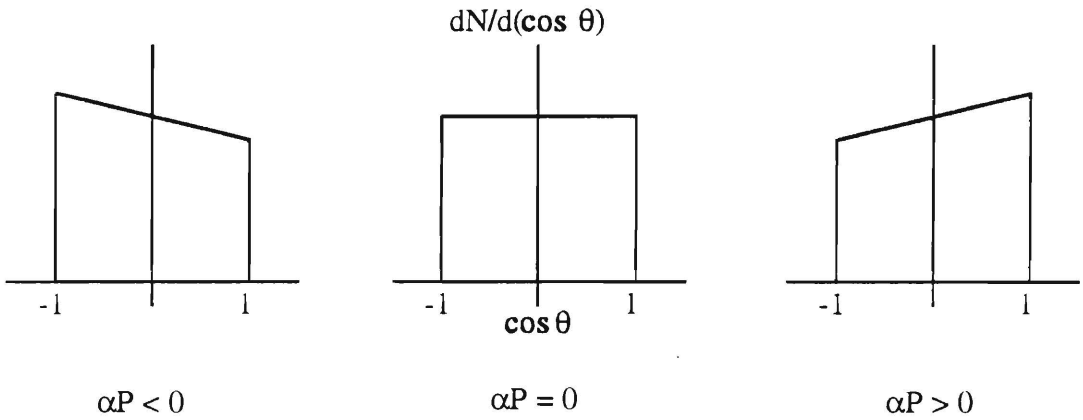

Figure 4.1 $(1+\alpha P \cos\theta)$ vs. $\cos\theta$ for $\alpha P < 0$, $\alpha P = 0$, $\alpha P > 0$.

with $A^{\pm}_j(\cos\theta)$ being the acceptance functions for positive and negative production angles. The acceptance functions differed not because the apparatus had changed, but because the Σ^- beam was not quite the same--having different targeting--at positive and at negative angles and, therefore, would probe the spectrometer apertures differently. This difference was small, however. For an example of this difference see Figure 3.6 which depicts the projections of the parent track at the exit of the collimator for the positive and negative production angle cases. The actual $\cos\theta$ distributions are shown in Figures 4.2 and 4.3 and 4.4. Since α**P** is small in this case, the plots show approximately the acceptance of the spectrometer. A short reflection reveals the reasons behind their shapes. Thus, the dip in the z distribution at $\cos\theta=-1$ and the dips in the x and y distributions at $\cos\theta=0$ correspond to the case when the π^- was going backward and at a very small angle along the z axis in the Σ^- rest frame. (Note that because of the high β, the Σ^- rest frame was approximately the same as the lab rest frame: its axes differed from the lab's by less than 2 mrad.) This means that, in

the lab frame, the π^- was very soft (and the undetected neutron, very hard) and would most likely be stopped inside magnet M2. The cosθ distribution in the y direction dipped around the cosθ=±1 regions while the one in x peaked there because the rectangular apertures of the chambers and magnet M2 had larger horizontal than vertical dimensions.

Assuming that the acceptance functions for the positive and negative angles are the same, a simple analysis can be done to get a value for $\alpha\mathbf{P}$. This analysis hinges on the fact that the direction of the polarization P will reverse when the production angle is flipped from positive to negative: this means the slope of the cosθ distributions will change sign. Thus any difference between the cosθ distributions for the positive and negative production angles is indicative of a polarization signal. More precisely, the bin by bin difference between the distributions is:

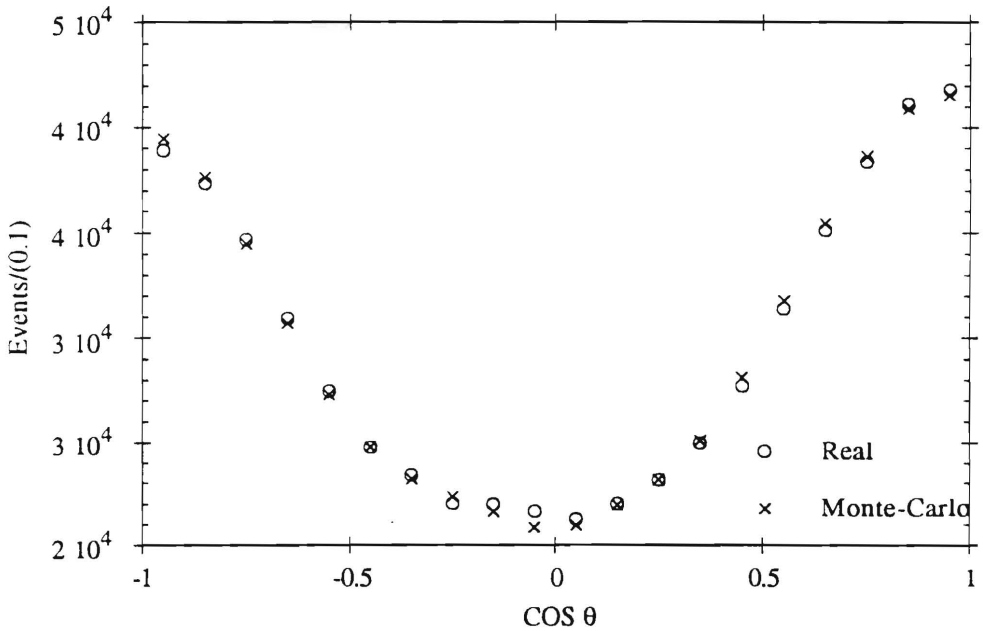

Figure 4.2 $\text{Cos}\theta_X$ distribution (real events and internal monte-carlo events) for negative production angle.

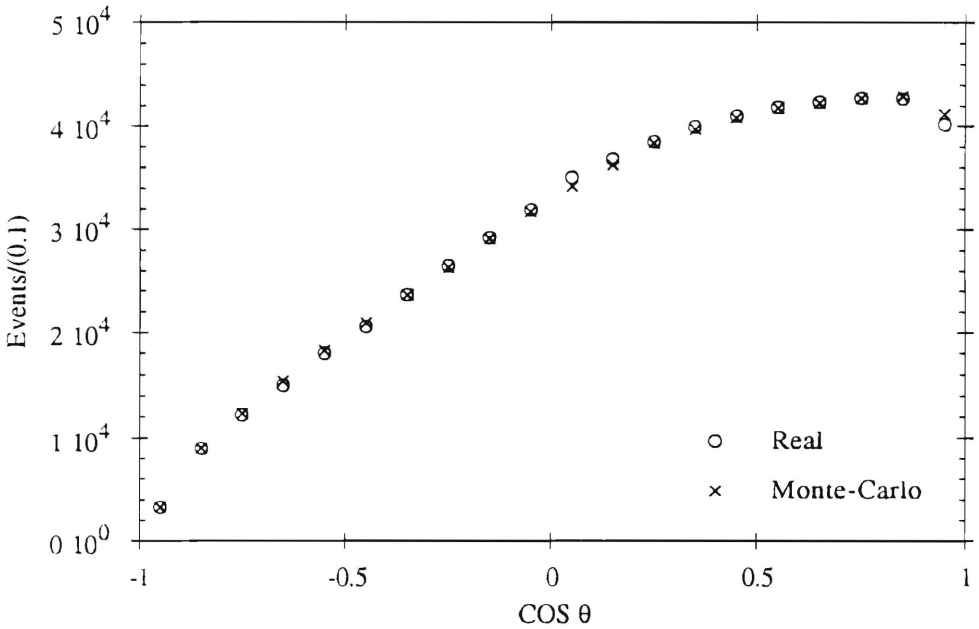

Figure 4.3 $\cos\theta_z$ distribution (real events and internal monte-carlo events) for negative production angle.

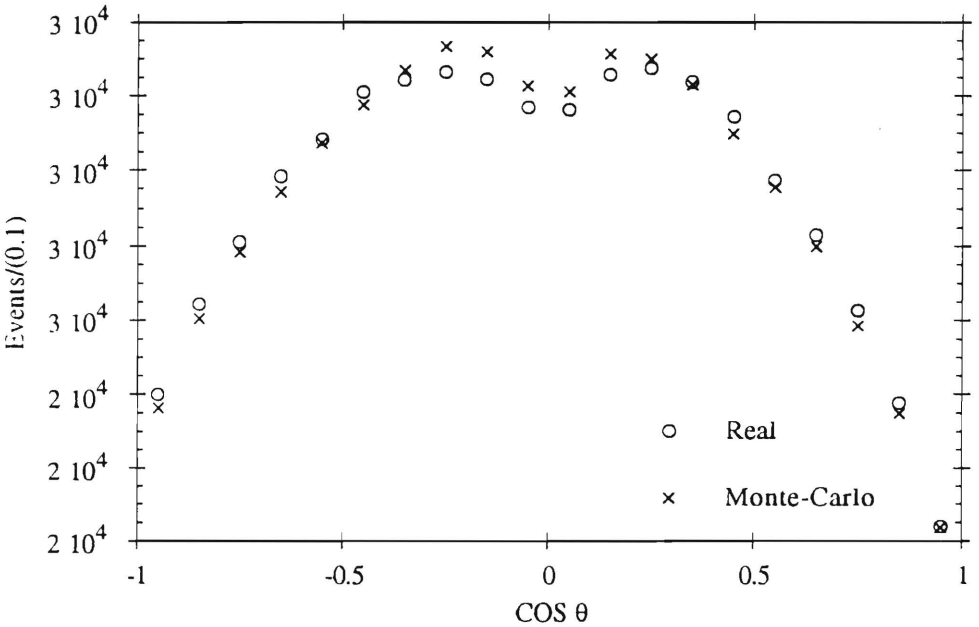

Figure 4.4 $\cos\theta_y$ distribution (real events and internal monte-carlo events) for negative production angle.

$$R = \frac{\Delta N_j^+ - \Delta N_j^-}{\Delta N_j^+ + \Delta N_j^-}$$

$$= \frac{A_j^+\left(1 + \alpha P_j \cos\theta_j\right) - A_j^-\left(1 - \alpha P_j \cos\theta_j\right)}{A_j^+\left(1 + \alpha P_j \cos\theta_j\right) + A_j^-\left(1 - \alpha P_j \cos\theta_j\right)} \tag{4.14}$$

$$= \alpha P_j \cos\theta_j$$

since $A_j^+ = A_j^-$ by assumption.

A plot of R versus $\cos\theta_j$ would now look like Figure 4.1 with R on the ordinate instead of $dN/d\cos\theta$. The slope of the plot would then give the product αP_j, which is the measurement desired.

4.2.2 Hybrid Monte-Carlo Method

The graphical method described above has the advantage of simplicity. On the other hand, that very simplicity implies some degree of crudeness. For one, it depends to some extent on the binning procedure. For another, there are effects that are production-angle dependent, that change sign when the production angle is flipped, just like a real polarization signal would. Examples are targeting effects such as that illustrated by Figure 3.6. These would induce a false polarization signal if the graphical method is used (c.f. the discussion of section 5.2 in the next chapter). To remedy these deficiencies and get a more accurate answer for the polarization, a hybrid (also referred to as internal) monte-carlo procedure described below could be used.

The philosophy of the hybrid monte-carlo method[22] is to simulate only variables that do directly influence the particular physical result under study and to take variables that do not from the data itself. This is in contrast to the standard monte-carlo practice of simulating as many known variables in an experiment as practical. Thus, for the immediate objective of unfolding the acceptance function from

the $\cos\theta_j$ distribution and thereby extracting αP_j, the variable of interest, $\cos\theta_j$, was generated randomly (with a uniform distribution) while all other incidental variables pertaining to a fake event, such as momentum, were taken from the real event. The fake event was then made to go through a software model of the spectrometer and reconstructed by the same reconstruction program, so that it effectively measured the geometric and reconstruction acceptance of the experiment. By requiring (via a weighting factor) the final monte-carlo distribution of $\cos\theta_j$ to be the same as the real distribution, the signal αP_j can then be extracted.

The monte-carlo took from the real event the decay vertex position, the momentum vector of the Σ^-, and the magnitude and azimuthal angle of the π^- in the Σ^- rest frame, but generated the $\cos\theta$ of the latter from a uniform distribution in the range [-1,1]. ($\cos\theta$ was alternately defined with respect to the x, y, and z axis, so as to measure all three components, P_j, of the polarization vector. The discussion following is confined to one choice of axis and the subscript j will be omitted for simplicity). It then boosted the π^- momentum vector back into the lab frame, and generated from it hit positions in a software model of the chambers and SSDs, complete with inefficient wires. These hits were then treated just like data from a real event and passed on to the analysis program if they satisfied the normal event selection and cuts, and if they observed the geometrical boundaries of a software version of all the spectrometer apertures. Fake events were generated (up to 200 tries maximum) until five (this number was found to be sufficient to model the data and its statistical uncertainty without introducing additional uncertainties) had been accepted per real event.

Because the fake events had to go through the same spectrometer's acceptance and analysis program's limitations as real events, the final fake reconstructed $\cos\theta$ distribution would no longer echo the original uniformly generated distribution, but would instead reflect the inherent acceptances of the apparatus and analysis program.

When the monte-carlo and the real-event distribution in $\cos\theta$ are compared, any difference between the two distributions is attributable to the fact that the real

distribution has a non-zero polarization. To do this comparison formally and extract the polarization signal in the process, the monte-carlo distribution is parametrized with a weighting factor

$$W = \frac{1 + \alpha P_f \cos\theta_f}{1 + \alpha P_r \cos\theta_r} \tag{4.15}$$

where subscript f signifies parameters of a fake event, and r a real event. The denominator "depolarizes" the fake sample: since the real data used to generate the fake events might be polarized already from the start, their polarization must be removed so it won't be mistaken as part of the measured acceptance. The numerator anticipates the need to "polarize" the fake sample after the acceptance function is found: by requiring the fake distribution to match the real distribution through an adjustment of αP in a χ^2 fit, the polarization signal can be extracted. Noting that after the fit, $\alpha P_f = \alpha P_r$, W can be expanded in a Taylor series in αP

$$W = 1 + \sum_i (-\alpha P)^i (\cos\theta_r)^{i-1} (\cos\theta_r - \cos\theta_f) \tag{4.16}$$

In this analysis, only four terms were kept. The result is an analytic function of αP that can be used in a χ^2 fit of the real $\cos\theta$ distribution.

In practice, the $\cos\theta$ distributions, fake and real, were divided into bins J (J=1,...,20). The χ^2 function was then evaluated bin by bin as

$$\chi^2(J,P) = \frac{\left(N_r(J) - \frac{N_f(J)}{N_0} \right)^2}{N_r} \tag{4.17}$$

where $N_r(J)$, $N_f(J)$ are the number of real and fake events with $\cos\theta$ falling in bin J respectively, and N_0 (=5) is the factor that normalized $N_f(J)$ to $N_r(J)$. The distribution $N_f(J)$ was

$$N_f(J) = C_0(J) + \sum_i C(J,P)\left(-\alpha P(J)\right)^i \tag{4.18}$$

where

$$C_0(J) = \sum_f 1 \tag{4.19}$$

and

$$C(J,P) = \sum_f (\cos\theta_r)^{i-1}(\cos\theta_r - \cos\theta_f) \tag{4.20}$$

These coefficients of expansion could, in a single pass of the data, be calculated and accumulated for each bin J. The asymmetry, αP, can then be obtained by minimizing the total χ^2,

$$\chi^2(P) = \sum_J \chi^2(J,P) \tag{4.21}$$

as a function of αP. The error in the value of αP obtained this way was given by the change in αP when the χ^2 changed from its minimum value by one unit.

4.2.3 Bias

Assuming that all of the acceptances have been taken care of by the hybrid monte-carlo, the asymmetry, αP, could be determined equally well from either the positive or negative production angle data sets.

In fact, inevitably not every acceptance effects could be accounted for. These remaining unaccounted for acceptances, lumped together under the heading, *bias*, are assumed to figure into the measured asymmetries as a constant independent of production angles:

$$\alpha P^{\pm} = \pm \alpha P + B \tag{4.22}$$

where $\alpha P^{\pm}$ are the experimentally measured asymmetries at positive and negative production angles, αP is the true asymmetry, which is independent of production angles, and B is the bias.

Under this assumption, the sums and differences of the measured asymmetries $\alpha P^{\pm}$ give the real polarization and biases, respectively:

$$\alpha P = \frac{\alpha P^{+} - \alpha P^{-}}{2}$$

$$B = \frac{\alpha P^{+} + \alpha P^{-}}{2} \tag{4.23}$$

Questions may be raised as to the plausibility of the assumption underlying this bias cancellation method--namely that the bias is independent of production angle while the polarization changes oppositely with a reversal of production angle. This is a legitimate question for the spin-transfer method since the production angle is defined here with respect to the first target, while the hyperon production of interest occurs at the second target. It is not so obvious that angle-related effects would still obtain. But in fact they do. An example is the P_y distribution at the second target mentioned previously. Figure 3.6b shows that the distribution indeed does change predictably

when the production angle is reversed, although not as much as it would have had the distribution been calculated for the first target.

A more subtle question is whether the magnitude of the changes are exactly equal so as to warrant the perfect cancellation postulated. The answer to that, unfortunately, is that they probably do not at the 1% level. This remains the Achilles heel of this method even when spin-transfer is not used (only one production target). This is because even in the most ideal of situations, there still remains the specter of statistical fluctuations, which can be reduced but never completely eliminated. Inevitably, the $\cos\theta$ distribution will have random fluctuations that will contribute to the bias. But hopefully with a large sample, this can be reduced to a negligible level.

4.3 The Grand χ^2 Fit

Statistical fluctuations also affect the final analysis of polarization and magnetic moment in another way. It has to do with the fact that data analysis often proceeds with a dividing, or binning, of the data sample into smaller groups or bins (e.g. momentum bins, or $\cos\theta$ bins). Sometimes this is done intentionally to reveal and accommodate real dependencies (e.g. the momentum dependence of the polarization) between variables, but often it is just plain necessary because of the inherent statistical spread of the data.

The problem is that there should be only one value for a fundamental physical result like the magnetic moment, whereas the binning procedure artificially creates many. One can take an average over the bins to obtain a single reasonable value for the physical variable. It is much better, however, to assume a priori the existence of a single value for the variable and then do a least-square--the so-called grand χ^2--fit of the binned data to this value.

The χ^2 function used in the minimization is of the form

$$\chi^2 = \sum_{jB} \left\{ \frac{\left[A_x(j) - B_x(j) \pm P(j)\cos(\Delta\phi_R(B))\right]^2}{\sigma_x^{\,2}(j)} + \frac{\left[A_z(j) - B_z(j) \pm P(j)\sin(\Delta\phi_R(B))\right]^2}{\sigma_z^{\,2}(j)} \right\} \tag{4.24}$$

where A and σ are the measured asymmetry and its statistical uncertainty; j indexes the particular binning variable (e.g. momentum); and the precession angle $\Delta\phi_R(B)$, is a function of the magnetic moment (via the g factor) and field integral

$$\Delta\phi_R(B) = \frac{1}{\beta}\left(g\mu_0 - \frac{e}{m}\right)\int |\mathbf{B}| \cdot dl \tag{4.25}$$

If there are a priori reasons (perhaps from the graphical method) to believe that the data is polarized, the fit can be done with $\Delta\phi_R$ as a free parameter. The outcome of the fit would then be the biases, B_X and B_Z; the polarization at target, P; and $\Delta\phi_R$, whence comes a measurement of the magnetic moment.

The fit can also be done with $\Delta\phi_R(B)$ evaluated at the world average value for the g factor (magnetic moment) of the Σ^-. In other words, the magnetic moment is fixed a priori by hand at the world value. No assumption is made regarding the state of polarization of the data. The fit would then give measurements of the biases B and polarization at target P.

CHAPTER 5

RESULTS AND CONCLUSION

The results for the asymmetries, αP, and the biases, B, that follow from applying the methods outlined in the last chapter to the Σ^- data will be described in this chapter. Over all, the data does not seem to be significantly polarized--if it is polarized at all--to warrant a measurement of the Σ^- magnetic moment.

5.1 Results--Graphical Method

According to the discussion of the last chapter, a plot of the ratio R_j versus $\cos\theta_j$ should be a straight line with slope αP_j. Figure 5.1 shows plots of R_x and R_z (R_y is experimentally misleading--c.f. Section 5.3--and theoretically zero as was discussed in section 1.1) for the data set at -450A sweeper current, and Figure 5.2, for the -1000A (the -750A data set was statistically insignificant and was ignored--c.f. Table 3.3). Note that to make these plots, the positive production angle data set was normalized to the negative one.

Also, two mixtures, each of which has equal number of events from the positive and events from the negative production angle data, were made from the -450A sample and analyzed just as if they were normal data samples. The resulting polarization should be zero because the net asymmetry for each mixture is zero. Figure 5.3 shows a plot of the ratio R_j for the mixture.

To make the comparison between the normal data set and the mixture data set for -450A even clearer, their respective plots have been superimposed in Figure 5.4. As can be seen, with the exception of a few data points, they match each other very closely within allowable statistical errors. The offhand implication based just on this cursory graphical view of the data is that the polarization of the normal data set is close to zero.

For concrete numbers, linear regression fits of the data in Figures 5.1-3 to the equation $R_j=\alpha P_j \cos\theta_j$ were done. The results are shown in Tables 5.1 and 5.2. The fits gave polarization signals for all three samples (-450A, -1000A, and the mixture at -450A) that are consistent with zero, being more or less only 1.5 standard deviations away from zero.

Data Set	αP_x	P_x	χ^2
-450A	-0.0008 ± 0.0014	-0.012 ± 0.020	17.1
-1000A	-0.0071 ± 0.0041	-0.105 ± 0.060	14.1
MIXTURE (-450A)	0.0002 ± 0.0014	0.003 ± 0.020	19.5
	αP_z	P_z	χ^2
-450A	0.0021 ± 0.0017	0.029 ± 0.025	18.8
-1000A	0.0012 ± 0.0046	0.018 ± 0.068	14.7
MIXTURE (-450A)	-0.0042 ± 0.0025	-0.061 ± 0.037	49.9

Table 5.1 Linear regression fits of the data of the graphs of Figures 5.1-3 to $R_j=\alpha P_j \cos\theta_j$. The number of degrees of freedom is 19.

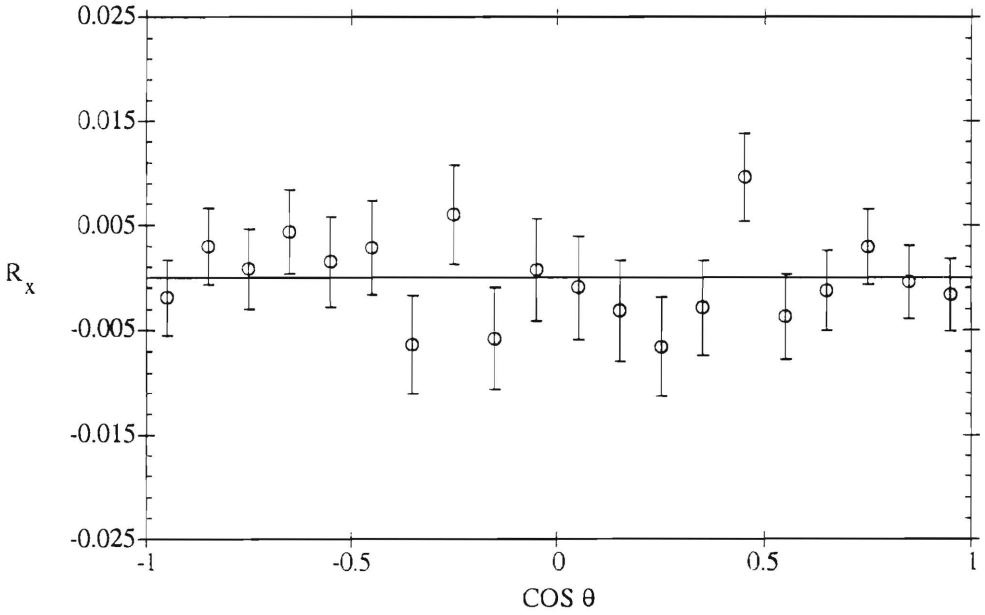

(a)

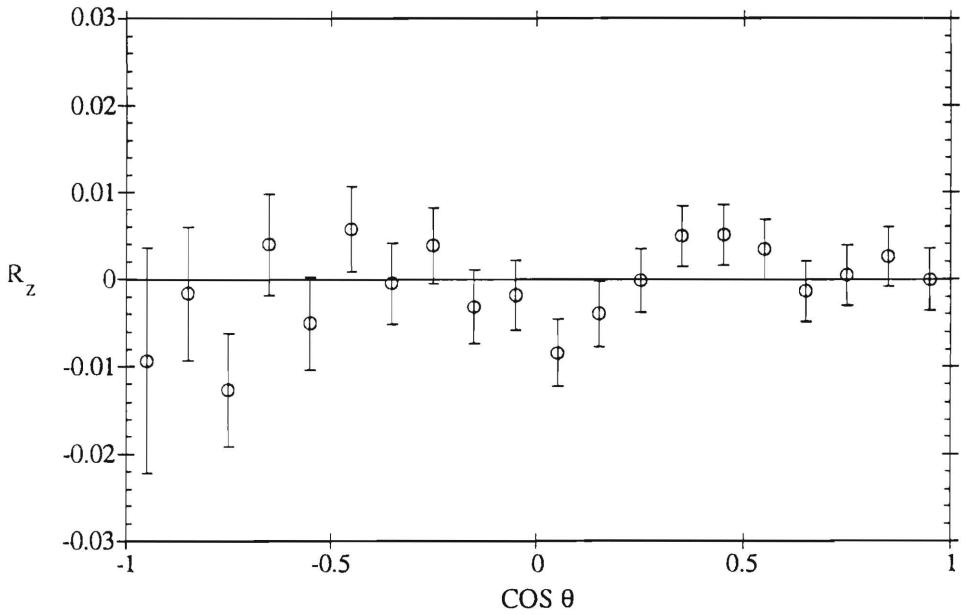

(b)

Figure 5.1 Ratio R for (a) x view (b) z view, for the -450A data set.

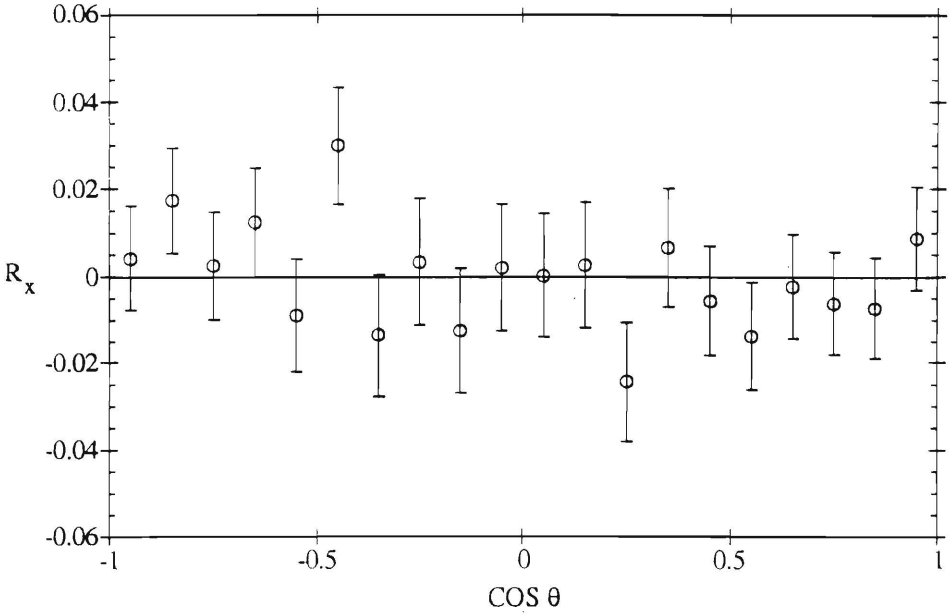

(a)

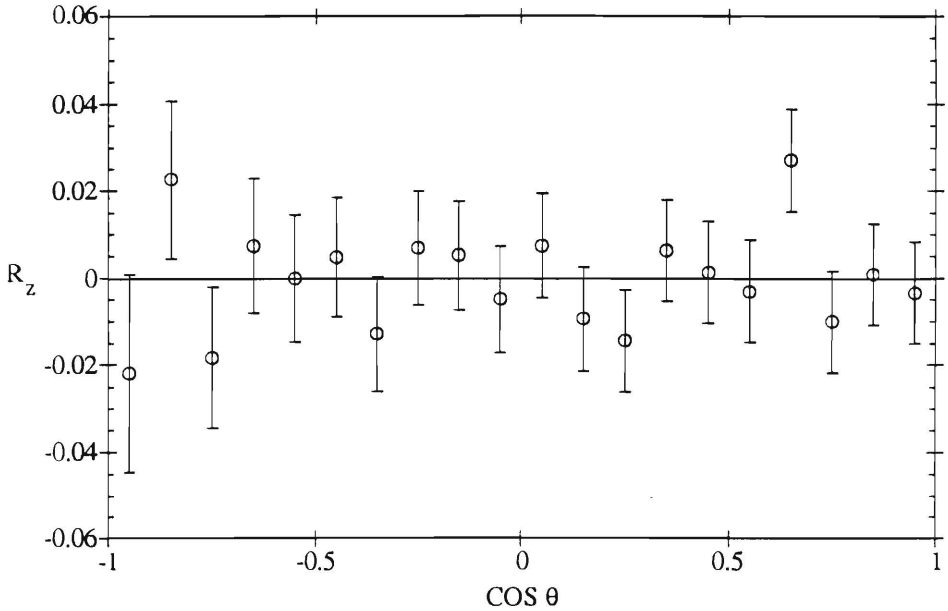

(b)

Figure 5.2 Ratio R for (a) x view (b) z view, for the -1000A data set.

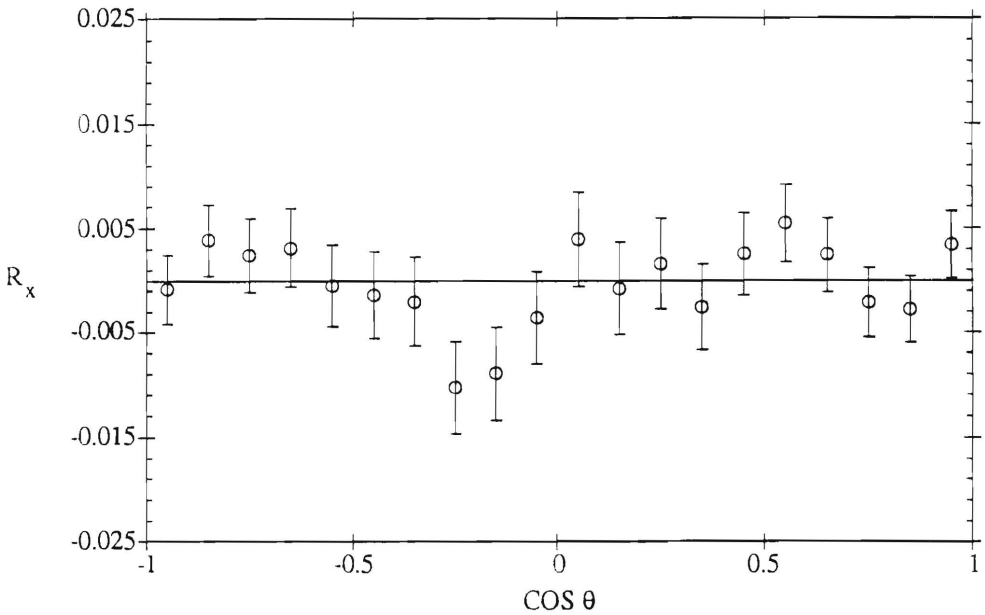

(a)

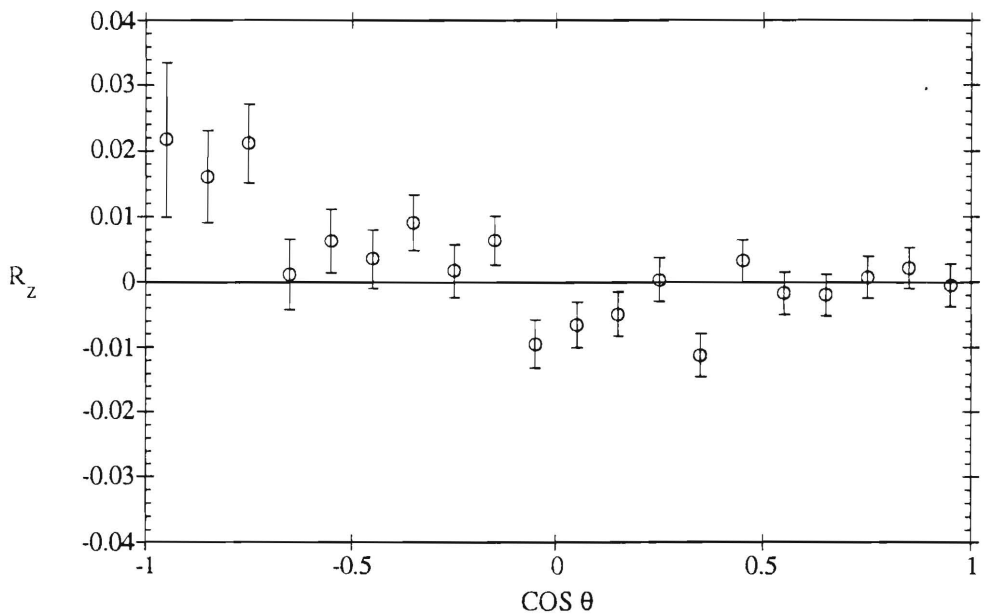

(b)

Figure 5.3 Ratio R for (a) x view (b) z view, for the mixtures of equal parts from the positive and the negative angle data sets (-450A)

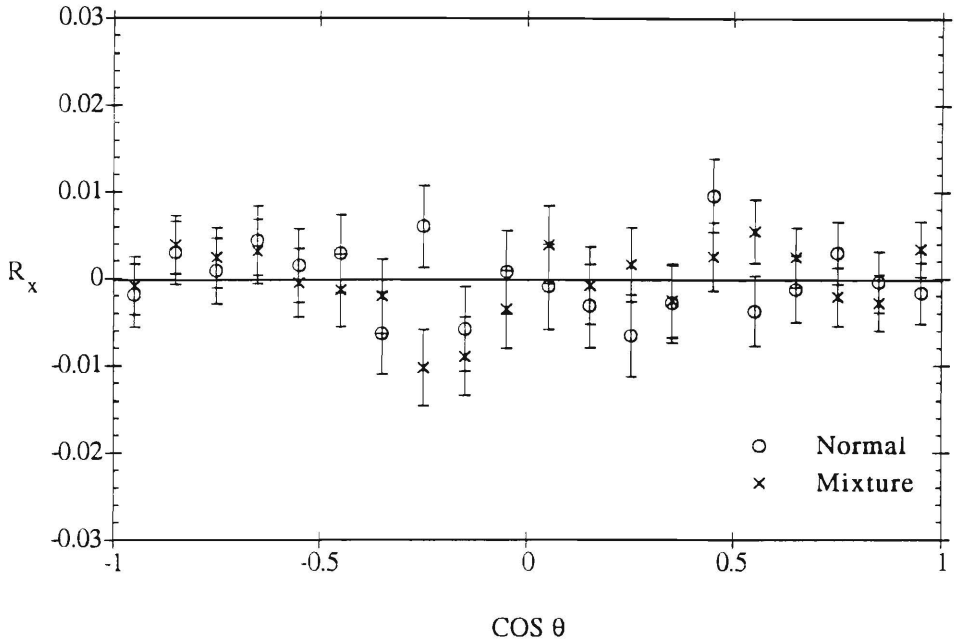

(a)

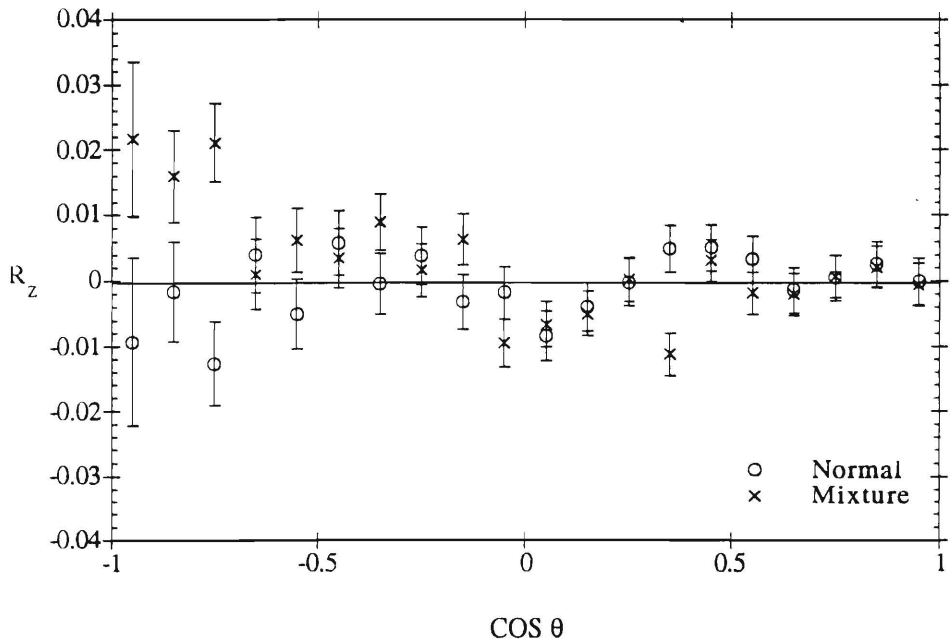

(b)

Figure 5.4 Comparison of the ratio R for (a) x view (b) z view, between the normal data set and the mixture data set of equal parts of positive and negative angle events (all data at -450A).

Data Set	$\lvert\alpha P\rvert$	$\lvert P\rvert$
-450A	0.0023 ± 0.0017	3 ± 2%
-1000A	0.0073 ± 0.0041	11 ± 6%
MIXTURE (-450A)	0.0042 ± 0.0025	6 ± 4%

Table 5.2 Results for the magnitude of the asymmetry $\lvert\alpha P\rvert$ and polarization $\lvert P\rvert$ that follow from the linear regression fits of Table 5.1.

5.2 A Digression: Graphical Method and the y Component

Only the x and z components of the polarization were considered above. This is because by parity conservation, the y component of the polarization theoretically should be zero (c.f. Section 1.1). An examination of the y component at this point can serve as a consistency check on the methodology.

Figure 5.5 is an R_j versus $\cos\theta_j$ plot for j=y. It shows unmistakably that indeed there is a y polarization signal. The signal measured, namely the product αP_y, is $\alpha P_y = 0.025$, yielding a y polarization signal of 37 % !

Does this mean the method is faulty? Fortunately not. In fact, the method is admirably doing its job, namely, to measure any asymmetries that change with a change in production angle. In this instance, the asymmetry measured is caused by a targeting asymmetry. Recall Figure 3.6b: the y distribution of the beam at the collimator exit was definitely different for positive and for negative production angle. Thus, because the beam peaked toward $P_y > 0$ for a positive production angle, there were more events in the $\cos\theta > 0$ region. Similarly, the number of events in the $\cos\theta < 0$ region were enhanced for a negative production angle. The net effect was that $R = (\Delta N^+ - \Delta N^-)/(\Delta N^+ + \Delta N^-)$ was positive, giving a false y polarization signal in apparent violation of parity conservation.

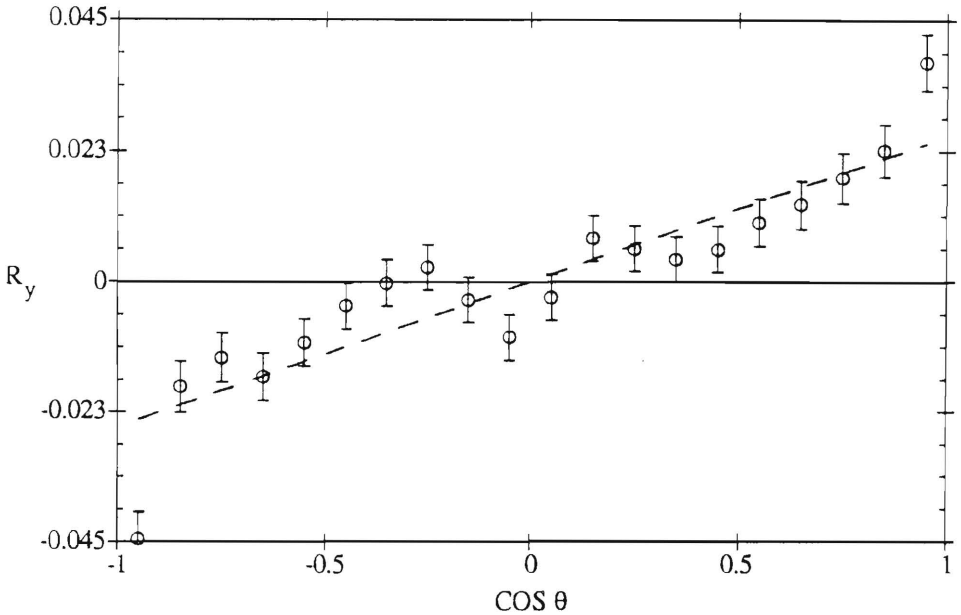

Figure 5.5 Ratio R for y view for -450A data set.

That the false signal is merely a production-angle dependent, targetting effect is further corroborated by Figure 5.6 which shows R_y for the mixture data set where ΔN^+ and ΔN^- each contains equal parts of positive and negative angle data. Because any production-angle dependent asymmetries would be obliterated by the mixing, as expected, R_y here is indeed zero.

Effectively, targeting effects result in acceptances at positive and negative production angles that are not exactly the same because the targeting distributions were different and hence the beam would see and sample different parts of the spectrometer in each case. But this is exactly what the hybrid monte-carlo is designed for: to model exactly the acceptance the beam sees. And indeed, the result in the next section confirms not only that the y component of the polarization is zero, but also that the data as a whole has a polarization consistent with zero.

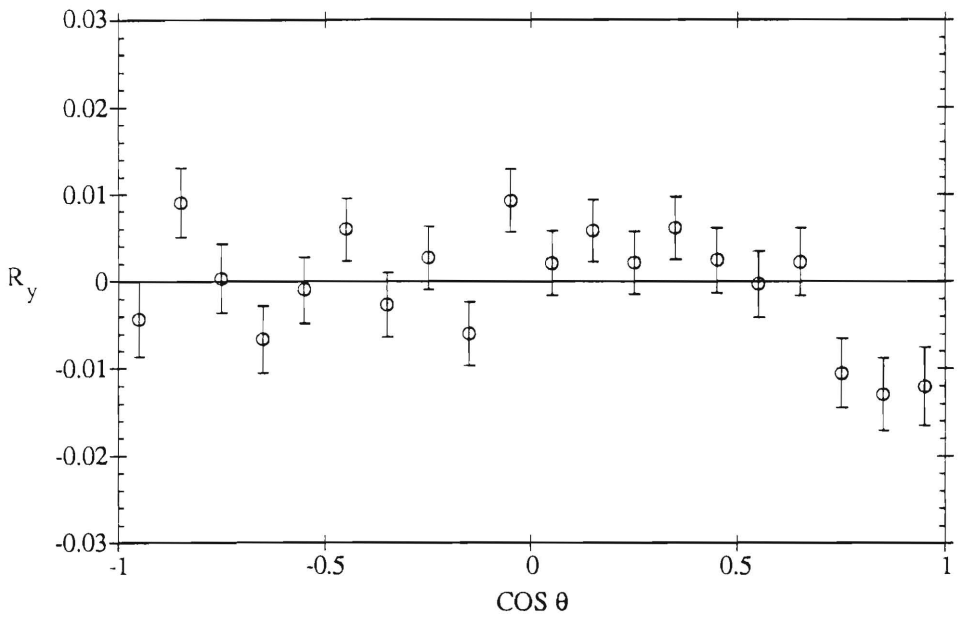

Figure 5.6 Ratio R for y view for mixtures of equal parts positive and negative production angle from the -450A data set.

5.3 Results--Hybrid Monte-Carlo Method

The results (Table 5.3) from applying the more sophisticated hybrid monte-carlo method to the data more or less reflect those obtained with the cruder graphical method of the previous two sections. First, as was advertised in the last paragraph, the y component of the polarization is indeed consistent with zero. Second, the magnitude of the polarization (calculated with the y component taken to be zero in Table 5.4) is also consistent with zero for all data sets. Note that in Table 5.4 an estimated systematic error was given for the measurements. This was obtained by varying the event selection criteria and observing changes in the measurement results.

The x bias computed by the hybrid program is surprisingly small, while the z bias is rather large in comparison with the polarization signal, but still quite typical. The values of these biases also agree with those obtained from a sample of zero milli-

radian data (i.e. where the primary proton beam struck the first target at 0 mrad, instead of at ±2 mrad) which should have no polarization.

Data Set	Momentum (GeV/c)	View	Polarization αP	Bias B	χ^2 Positive	χ^2 Negative
		x	-0.0006 ± 0.0016	-0.0004	102	61
-450A	321	y	-0.0028 ± 0.0018	0.0002	171	133
		z	-0.0026 ± 0.0023	0.0228	101	156
		x	-0.0047 ± 0.0045	0.0008	95	79
-1000A	410	y	-0.0089 ± 0.0050	0.0060	34	36
		z	-0.0082 ± 0.0058	0.0317	62	64
MIXTURE		x	-0.0005 ± 0.0017	-0.0004	61	96
(-450A)	321	y	0.0038 ± 0.0020	0.0018	93	205
		z	-0.0036 ± 0.0024	0.0217	53	195

Table 5.3 Results for the components of the polarizations, biases, and χ^2 for the positive and negative production angle data (number of degrees of freedom is 20) for the hybrid monte-carlo method, calculated with Equation 4.23. Also shown is the average Σ^- momentum for each sample.

Data set	$\lvert\alpha P\rvert$	$\lvert P\rvert$
-450A	0.0027 ± 0.0022 ± 0.0012	3.9 ± 3.2 ± 1.8%
-1000A	0.0095 ± 0.0055 ± 0.0014	13.9 ± 8.1 ± 2.0%
MIXTURE(-450A)	0.0037 ± 0.0024 ± 0.0012	5.4 ± 3.5 ± 1.8%

Table 5.4 Results for the magnitude of the polarization signal at target, $\lvert\alpha P\rvert$, using the hybrid monte-carlo method. For each measurement, the first error is statistical and the second, systematic.

Table 5.5 displays the results for the precession angle and magnetic moment for the different data samples using the hybrid monte-carlo method. Note that for each sample, there are four distinct lowest-order solutions for the precession angle ϕ and for the magnetic moment. This fourfold ambiguity arises because although the initial polarization is constrained to be along the x axis, it can be either in the positive or negative direction; further, the final polarization could have been obtained from the initial polarization by precessing either clockwise or counter-clockwise. (Of course, because $\phi = \tan^{-1}(P_x/P_z)$, modulo 360° higher-order solutions of these four basic ones also exist.)

Data Set	ϕ	$\Delta\phi$	g/2	Δg/2	μ (n.m.)	$\Delta\mu$(n.m.)
	77.3°		*1.37*		*-1.07*	
450A	*-102.7°*	*17.4°*	*0.51*	*0.08*	*-0.40*	*0.07*
	257.3°		2.24		-1.76	
	-282.7°		-0.36		0.28	
	60.3°		*1.22*		*-0.95*	
1000A	*-119.7°*	*29.3°*	*0.57*	*0.11*	*-0.45*	*0.08*
	-299.7°		-0.07		0.06	
	240.3°		1.86		-1.46	
	81.4°		1.39		-1.09	
Mixture	-278.6°	27.0°	-0.34	0.13	0.27	0.10
(450A)	261.5°		2.26		-1.77	
	-98.5°		0.53		-0.41	

Table 5.5 Results for the precession angle ϕ and its error; the g/2 ratio and error; and the magnetic moment μ and error from the hybrid monte-carlo method.

In principle, the two data samples at -450A and at -1000A taken together should be able to resolve this fourfold ambiguity. This follows since Equation 1.9

implies not only that the two samples must precess in the same direction but also that the sample with the larger $\int Bdl$ must precess by a larger amount. Further, the amount of precession for both samples must be consistent with the same value for g/2.

Tables 5.6 and 5.7 below show the results obtained from combining and fitting both the -450A and -1000A data samples together using the "grand-χ^2" described in the last section of the previous chapter. This was done first under the assumption that there is a polarization so that a measurement of the magnetic moment can be made (i.e. g/2 of the Σ^- was allowed to be a free parameter and an output of the fit). Then the fit was redone with no assumption regarding polarization and with the world average value for the magnetic moment of the Σ^- substituted in the grand-χ^2 expression (i.e. g/2 is fixed at world value; c.f. the discussion of equation 4.24).

Contrary to expectation, the fourfold ambiguity was not exactly broken. In the first fit, two solutions (A & B) for the magnetic moment were obtained (μ = -0.43 ± 0.08 n.m. and μ = -0.97 ± 0.08 n.m., respectively), both with comparably good χ^2. Compare to the world average value (μ = -1.157 ± 0.025 n.m.), the second solution B

Condition	Solution	Sample	αP	x bias	z bias
g/2=free parameter	A	-450A	-0.0027 ± 0.0023	-0.0004 ± 0.0016	0.0228 ± 0.0023
		-1000A	-0.0092 ± 0.0055	0.0009 ± 0.0045	0.0316 ± 0.0058
	B	-450A	-0.0020 ± 0.0020	-0.0005 ± 0.0016	0.0228 ± 0.0023
		-1000A	-0.0096 ± 0.0055	0.0007 ± 0.0045	0.0317 ± 0.0058
g/2=world value		-450A	-0.0023 ± 0.0022	-0.0003 ± 0.0016	0.0228 ± 0.0023
		-1000A	-0.0005 ± 0.0051	0.0003 ± 0.0045	0.0308 ± 0.0058

Table 5.6 Results for the asymmetry αP, and the x and z biases when both the -450A and -1000A samples were fitted simultaneously using the "grand-χ^2". Two separate fits are shown: first, with g/2 being a free parameter and second, with g/2 set at the world value in the "grand-χ^2" expression of Equation 4.24. Two solutions (A & B) with equally good χ^2 were obtained from the first fit.

Condition	Solution	Sample	|P|	ϕ	μ (n.m.)	χ^2
g/2=free parameter	A	-450A	3.9 ± 3.4 %	-93.1 ± 26.8°	-0.43 ± 0.08	0.11
		-1000A	13.5 ± 8.1 %	-125.0 ± 26.8°		
	B	-450A	2.9 ± 2.9 %	50.0 ± 27.2°	-0.97 ± 0.08	0.46
		-1000A	14.1 ± 8.1 %	67.1 ± 27.2°		
g/2=world value		-450A	3.4 ± 3.3 %	*98.9°*	*-1.157*	3.4
		-1000A	0.7 ± 7.7 %	*132.9°*		

Table 5.7 Results for the polarization P, precession angle ϕ, and magnetic moment μ when both the -450A and -1000A samples were used in simultaneous fits using the "grand-χ^2". In the first fit, g/2 was allowed to be free in the expression of Equation 4.25. In the second fit, the values of g/2, or equivalently μ, and ϕ were fixed at world values given in the particle data book[21] and were used to obtain values for P and the biases shown in Table 5.6. The number of degrees of freedom is 1 for the first fit and 2 for the second. Note that two solutions (A & B) with equally good χ^2 were obtained from the first fit.

is the choice even though it is ≈2.5 standard deviations away. However, it has a higher χ^2 than the other solution. And for that reason, solution A is preferred.

The situation is depicted graphically in Figure 5.7. As it turned out, two pairs of points in Table 5.5 (italicized rows) approximately satisfy the ambiguity resolution conditions mentioned three paragraphs ago. The two solutions correspond to initial polarization vectors at target that point in opposite directions (see Figure 5.8). From the slopes of the graphs of Figure 5.7, the magnetic moments are $\mu = 0.42 \pm 0.02$ n.m. and $\mu=1.03 \pm 0.04$ n.m. corresponding to the hybrid monte-carlo solutions A and B respectively. Again, solution A is the preferred on the basis of its smaller χ^2 (which is distinctly much smaller than B, here in this graphical analysis).

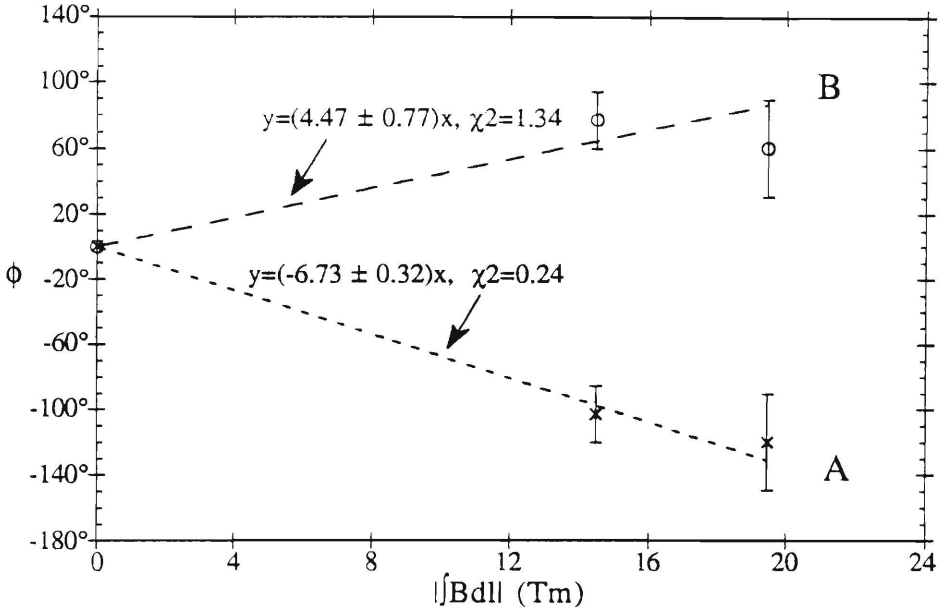

Figure 5.7 Precession angle versus field integral for the two solutions (A & B) found using the hybrid method. The equations of best fit and the corresponding χ^2 are also given. Note that, as a matter of course, the origin (0,0) is a point in the fit.

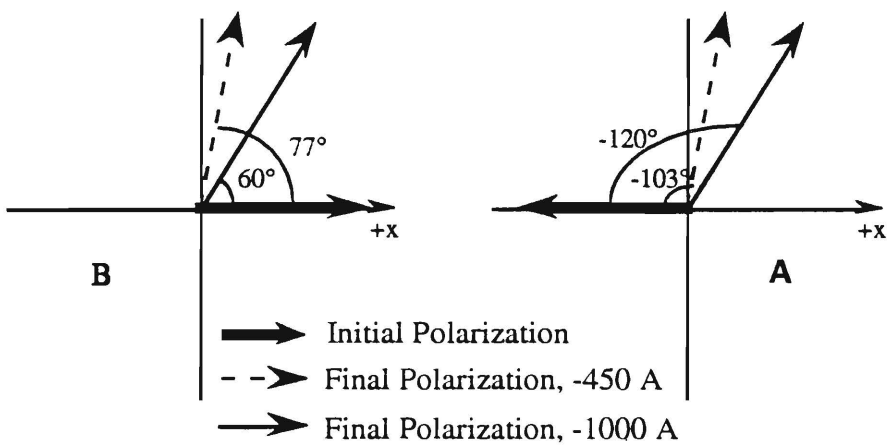

Figure 5.8 Final solutions A & B correspond to an unresolved ambiguity in the initial polarization direction at target. In principle, the final polarization vector of the larger field (-1000A) should precess more than that of the smaller field, so that solution A is the preferred; but because of limited angular resolution, B can also fit the data.

The reason for the existence of the ambiguity is evident from the graph: within statistical errors, solution B happens to be an average that can fit both $\int Bdl$ field values to one value of g/2. However, for this solution, the smaller $\int Bdl$ precessed much more than it should, and/or the larger $\int Bdl$ precessed much less than it should. In principle, the polarization vector of the larger field should always lead that of the smaller field. Solution A is the preferred in this view, since for this solution, the larger field precessed more than the smaller field as it should.

But, solution A for the magnetic moment is very far from the world average value. Solution A implies that the data does not fit the world value very well. This fact is corroborated by the results obtained for the second hybrid monte-carlo fit where the data is forced to fit the world value: the χ^2 (3.4 per 2 degrees of freedom) for the fit is not so good.

If solution A is given credence, then the only logical conclusion is that the assumption that the data is polarized is incorrect. And it must be concluded that the polarization signal for both the -450A and the -1000A sample is consistent with zero--which, statistically speaking, they are in fact (recall Table 5.4, and the fact that the results for both samples are consistent with the result for the MIXTURE sample, which should have exactly zero polarization by design). Also recall Table 5.3 where the individual components of the polarization are shown. Note that, for all intent and purposes, the x component is identical to zero. The z component contributes the largest part to the non-zero magnitude of the polarization, |P|. However, the large z bias, compared to the z signal (and compared to the very small x bias), casts doubt on the trustworthiness of the z polarization signal. At any rate, even these numbers indicate a polarization that is not very different from zero.

Any conclusion to the effect that the data is, in fact, unpolarized must be tempered with some caution, however. The ambiguity over solutions A and B amounts to an ambiguity in the direction of the initial polarization vector; which comes about because of an ambiguity over which final polarization vector leads the other; which, in turn, comes about because of the limited angular resolution in the

measurement of the precession angle. The final polarization vectors of solutions A and B overlap each other (Figures 5.7, 5.8, and Table 5.5) within their range of angular uncertainty.

It is clear from the results that it is not possible to conclude with definiteness whether the data is polarized or not. It is clear, however, that if it is polarized, the magnitude of the polarization is insignificantly small--too small to overcome the statistical limitation imposed by the marginal size of the sample and the very small α of the Σ^-: given the size of the sample (N ≈ half million events per production angle), the expected statistical error in the measurement of a component of the polarization, $\delta P = 1/(\alpha\sqrt{3/N})$, is of the order 4-5%. And the data indicates that the magnitude of the polarization is of the same order, if it is in fact polarized.

5.4 Conclusion

In summary, the polarization of Σ^- hyperons produced by the spin-transfer technique using a neutral beam on a copper target in inclusive reactions of the type, *neutral + Cu* $\rightarrow$ Σ^- *hyperon + X*, has been measured at average Σ^- momenta 320 GeV/c and 410 GeV/c and found to be P = 3.9 ± 3.2 ± 1.8 % and P = 13.9 ± 8.1 ± 2.0 % respectively. These polarizations are not significantly different from zero to warrant a measurement of the Σ^- magnetic moment. In fact, inconsistencies in fitting the data to the magnetic moment would be resolved if the data is not polarized.

The predicted polarization of hyperon beams from the DeGrand-Miettenen model for spin-transfer reactions is summarized in Table 5.8.[23] In the table, ε and δ are model parameters related to the quark and diquark polarizations; they are constrained by experimental data for "standard" (i.e. non-spin-transfer) production polarization initiated by unpolarized beams to be roughly equal to within 20%. The polarization of the incoming neutral beam figures in as parameter d in the table.

Reaction	Predicted Asymmetry
$n \rightarrow \Sigma^-$	$1/3\ (\varepsilon + 2\delta + 2d)$
$\Lambda^0 \rightarrow \Sigma^-$	$1/6\ (-4\varepsilon + \delta + d)$
$\Xi^0 \rightarrow \Sigma^-$	$1/9\ (-3\varepsilon - 6\delta - 2d)$
$n \rightarrow \Xi^-$	$1/9\ (-3\varepsilon - 6\delta - 2d)$
$\Lambda^0 \rightarrow \Xi^-$	$1/6\ (-4\varepsilon + \delta + d)$
$\Xi^0 \rightarrow \Xi^-$	$1/3\ (\varepsilon + 2\delta + 2d)$
$n \rightarrow \Omega^-$	0
$\Lambda^0 \rightarrow \Omega^-$	$5/6\ (\varepsilon - \delta + d)$
$\Xi^0 \rightarrow \Omega^-$	$5/6\ (-\varepsilon + \delta + d)$

Table 5.8 Predicted polarization asymmetries for various spin-transfer reactions with a neutral beam. The parameter $\varepsilon \approx \delta$, and d is the polarization of the incoming beam. The predictions are given to first order in all the parameters.

It is clear from the table that in the case of the Ω^-, the two hyperon-initiated reactions give rise each to a positive asymmetry that is 5/6 times the polarization of the neutral beam. In experiment E756, it was observed that indeed the Ω^- produced by spin transfer has a polarization of the order of 11 ± 2 %.[3]

For the case of the Σ^-, it is not so clear what net polarization the neutral beam would produce. As can be seen from the table, the reaction $\Xi^0 \rightarrow \Sigma^-$ would produce Σ^- with a negative polarization, whereas the reaction $\Lambda^0 \rightarrow \Sigma^-$ could produce either a positive or a negative polarization depending on the relative magnitude of the parameters δ, ε, and d. Also, the reaction initiated by the neutron--which is present in abundant in the neutral beam--would produce a positive polarization. Some cancellation among these different reactions conceivably could have happened, resulting in the observed insignificant, if not zero, Σ^- polarization.

REFERENCES

1 G. Bunce *et al.*, Phys. Rev. Lett. **36**, 1133 (1976).

2 P.M.Ho *et al.*, Phys. Rev. Lett. **65**, 1713 (1990).

3 H.T.Diehl *et al.*, Phys. Rev. Lett., to be published.(1991).

4 C. Wilkinson *et al.*, Phys. Rev. Lett. **46**, 803 (1981).

5 C. Ankenbrandt *et al.*, Phys. Rev. Lett. **51**, 863 (1983).

5 K. Heller *et al.*, Phys. Rev. Lett. **51**, 2025 (1983).

6 L. Deck *et al.*, Phys. Rev. **D28**, 1 (1983).

7 Y. W. Wah *et al.*, Phys. Rev. Lett. **55**, 2551 (1985).

8 R. Rameika *et al.*, Phys. Rev. **D33**, 3172 (1986).

9 E. C. Dukes *et al.*, Phys. Lett. **193B**, 135 (1987).

10 L. H. Trost *et al.*, Phys. Rev. **D40**, 1703 (1989).

11 K. Heller *et al.*, Phys. Rev. Lett. **41**, 607 (1978).

12 F. Lomanno *et al.*, Phys. Lett. **96B**, 223 (1980).

13. B. Lundberg *et al.*, Phys. Rev. **D40**, 3557 (1989).

14. R. Rameika *et al.*, "Search for Polarization in Ξ^0 Hyperons", in High Energy Spin Physics, 126 (1982), AIP Proceedings of the 8th International Symposium.

15 V. Bargmann, L. Michel and V. L. Telegdi, Phys. Rev Lett. **2**, 435 (1959).

16. G. Zapalac *et al.*, Phys. Rev. Lett. **57**, 1526 (1986).

17 D. W. Hertzog *et al.*, Phys. Rev Lett **D37**, 1142 (1988).

18 T. DeGrand and H. I. Miettinen, Phys. Rev. **D23**, 1227 (1981), Phys. Rev. **D24**, 2419 (1981).

19 B. Andersson, G. Gustafson, and G. Ingelman, Phys. Lett. **85B**, 417 (1979).

20 J. Szwed, Phys. Lett. **105B**, 403 (1981).

21 Particle Data Group. Review of Particle Properties., Phys. Lett., **239B**,1 (1990).

22 G. Bunce, Nucl. Instrum. Methods **172**, 553 (1980).

23 T.A. DeGrand, et al. Phys. Rev. **D32**, 2445 (1985)